

1 Quantifying the Impact of SST Feedback Frequency on the 2 Madden-Julian Oscillation Simulations

3 Yung-Yao Lan¹, Huang-Hsiung Hsu¹, and Wan-Ling Tseng²

4 ¹Research Center for Environmental Changes, Academia Sinica, Taipei 11529, Taiwan

5 ²Ocean Center, National Taiwan University, Taipei 10617, Taiwan

6 *Correspondence to:* Huang-Hsiung Hsu (hhhsu@gate.sinica.edu.tw)

7 8 **Abstract**

9 This study uses the CAM5 coupled to a 1-d ocean model to investigate the effects
10 of intraseasonal SST feedback frequency on the Madden-Julian Oscillation (MJO)
11 simulation with intervals at 30 minutes, 1, 3, 6, 12, 18, 24, and 30 days. The large-scale
12 nature of the MJO in simulations remains intact with decreasing feedback frequency,
13 although becoming increasingly unrealistic in both structure and amplitude, until
14 1/30days when the intraseasonal fluctuations are overwhelmingly dominated by
15 unorganized small-scale perturbations in both atmosphere and ocean, as well as at the
16 atmosphere-ocean interface where heat and energy are rigorously exchanged. The main
17 conclusion is less frequent the SST feedback, more unrealistic the simulations. Our
18 results suggest that spontaneous atmosphere-ocean interaction with high vertical
19 resolution in the ocean model is the key to the realistic simulation of the MJO and
20 should be properly implemented in climate models.

21 22 **1. Introduction**

23 The Madden-Julian Oscillation (MJO) is a large-scale tropical circulation that
24 propagates eastward from the tropical Indian Ocean (IO) to the western Pacific (WP)
25 with a periodicity of 30–80 days (Madden and Julian, 1972). In the Indo-Pacific region,
26 the MJO processes involve intraseasonal variability of sea surface temperature (SST)
27 (Chang et al., 2019; DeMott et al., 2014, 2015; Jiang et al., 2015, 2020; Krishnamurti
28 et al., 1998; Li et al., 2014; Li et al., 2020a; Newman et al., 2009; Pei et al., 2018; Stan,

29 2018; Tseng et al., 2015). The tropical air–sea interaction, influenced by the upper ocean,
30 plays a crucial role in determining MJO characteristics due to the high heat capacity of
31 the upper ocean within the intraseasonal range, which acts as a significant heat source
32 for atmospheric variability (Watterson 2002; Sobel and Gildor 2003; Maloney and
33 Sobel 2004; Sobel et al. 2010; Liang and Du, 2022).

34 Analyzing the mechanism of the intraseasonal oscillation (ISO) reveals that heat
35 fluxes play a critical role in the development of intraseasonal SST variability (Hong et
36 al., 2017; Liang et al., 2018). As demonstrated in Fu et al. (2017), underestimation
37 (overestimation) of the air–sea coupling's impact on MJO simulations occurs when it is
38 weak (strong) in the intraseasonal SST variability. Simulation improvements in the
39 eastward propagation and regulation of MJO periodicity in the coupled models can be
40 attributed to several factors such as enhanced low-level convergence and convective
41 instability to the east of convection, as well as enhanced latent heat fluxes (Savarin and
42 Chen, 2022) and SST cooling to the west of convection (DeMott et al., 2014). SST
43 gradients have been found to induce patterns of mass convergence and divergence
44 within the marine boundary layer (MBL), initiating atmospheric convection (de Szoeke
45 and Maloney, 2020; Lambaerts et al., 2020).

46 Several recent studies have made significant progress in understanding the impact
47 of air–sea coupling on the MJO, particularly at sub-daily scales (e.g., DeMott et al.,
48 2015; Kim et al., 2018; Seo et al., 2014; Voltaire et al., 2022; Zhao and Nasuno, 2020).
49 However, there is relatively limited discussion on the effect of air–sea coupling from
50 few days to within half of the MJO period. Several studies have investigated the impact
51 of intraseasonal SST on the MJO by coupled or uncoupled models. (e.g., DeMott et al.,
52 2014; Gao et al., 2020b; Klingaman, and Demott, 2020; Pariyar et al., 2023; Stan, 2018).
53 Simulations using time-varying SSTs from coupled global climate model (CGCM) to
54 force the atmospheric general circulation model (AGCM) showed a reduced

55 intraseasonal SST variability, leading to weakened air–sea heat fluxes and eastward
56 propagation (DeMott et al., 2014; Gao et al., 2020b; Klingaman, and Demott, 2020;
57 Pariyar et al., 2023). Moreover, the absence of few days variability in SST promotes
58 the amplification of westward power associated with Rossby waves (Stan, 2018).

59 Incorporating two-way coupling between the ocean and atmosphere has been
60 proved valuable for simulating and predicting intraseasonal variability (e.g., DeMott et
61 al., 2014; Lan et al., 2022; Stan, 2018; Tseng et al., 2015, 2020). As demonstrated in
62 recent studies (e.g., Ge et al. 2017, Lan et al., 2022, Shinoda et al. 2021, and Tseng et
63 al. 2015, 2022), incorporating high vertical resolution near the ocean surface positively
64 influences the accurate representation of intraseasonal SST variability and enhances the
65 MJO prediction capabilities. However, how frequent is the coupling needed is still not
66 fully understood, considering the fact that the ocean and atmosphere could evolve in
67 distinct time scales. And, would the coupling frequency in numerical models influence
68 the accuracy of the MJO simulation?

69 In this study, we aim to investigate the specific effects of oceanic feedback
70 frequency (FF) through air–sea coupling on the atmospheric intraseasonal variability,
71 using the National Center for Atmospheric Research (NCAR) Community Atmosphere
72 Model 5.3 (CAM5.3) coupled with the single-column ocean model named Snow–Ice–
73 Thermocline (SIT). The coupled model is referred to as CAM5–SIT. The SIT model,
74 consisting of 41 vertical layers, enables the simulation of SST and upper-ocean
75 temperature variations with high vertical resolution (Lan et al., 2022). We have
76 demonstrated in previous studies that coupling the SIT significantly improved the MJO
77 simulations in several AGCMs (Tseng et al. 2015, 2022, Lan et al. 2022). The ability of
78 the SIT with extremely high-resolutions (i.e., 12 layers within the first 10.5 m) to well
79 resolve the upper ocean warm layer and the cool skin of the ocean surface was identified
80 as the main reason for the improved simulations.

81 The structure of this paper is organized as follows. Section 2 introduces the model,
82 data, methodology, and experiments employed in this study. The performance of the
83 CAM5–SIT models in simulating the MJO is discussed in Section 3, while Section 4
84 focuses on the impact of different configurations of sub-seasonal SST feedback
85 periodicity on MJO simulations. Finally, Section 5 presents the conclusions.

86

87 **2. Data, model experiments, and methodology**

88 **2.1 Observational data**

89 Observational data sets used in this study include precipitation from the Global
90 Precipitation Climatology Project (GPCP, 1° resolution, 1997–2010; Adler et al., 2003),
91 outgoing longwave radiation (OLR, 1° resolution, 1997–2010; Liebmann, 1996), and
92 daily SST (optimum interpolated SST, OISST, 0.25° resolution, 1989–2010; Banzon et
93 al., 2014) from the National Oceanic and Atmosphere Administration, and the fifth
94 generation ECMWF reanalysis (ERA5), with a resolution of 0.25° for the period of
95 1989–2020 (Hersbach and Dee, 2016). Various variables from ERA5 were considered,
96 including winds, vertical velocity, temperature, specific humidity, sea level pressure,
97 geopotential height, latent and sensible heat, and shortwave and longwave radiation.
98 For the initial conditions of the SIT, the SST data was obtained from the Hadley Centre
99 Sea Ice and Sea Surface Temperature dataset version 1 (HadISST1), with a resolution
100 of 1° for the period of 1982–2001 (Rayner et al., 2003). The ocean subsurface data,
101 including climatological ocean temperature, salinity, and currents in 40 layers, were
102 retrieved from the National Centers for Environmental Prediction (NCEP) Global
103 Ocean Data Assimilation System (GODAS) with a resolution of 0.5° for the period of
104 1980–2012 (Behringer and Xue, 2004). These data were used for a weak nudging
105 (Tseng et al. 2015 2022; Lan et al. 2022) in the SIT model.

106

107 2.2 Experimental design

108 In this study, we investigated the role of oceanic FF using coupled CAM5–SIT and
109 atmosphere-only CAM5 (A–CTL). Previous studies (Lan et al., 2022; Tseng et al., 2022)
110 have provided a detailed description of the every timestep coupling CAM5–SIT model
111 and its performance in simulating the MJO. Table 1 displays the experimental
112 configuration, incorporating monthly HadISST1 (uncoupled region) and ice
113 concentrations over a 30-year period centered around the year 2000 (F2000 compsets,
114 Rasch et al., 2019). Solar insolation, greenhouse gas and ozone concentrations, and
115 aerosol emissions representative of present-day conditions were prescribed. In the A–
116 CTL, observed monthly-mean SST around the year 2000 was prescribed to force the
117 CAM5. For the coupled simulations, we adjusted the Flux Coupler (CPL) restriction in
118 the Climate Earth System Model (CESM1; Hurrell et al., 2013) by implementing
119 asymmetric exchange frequencies between the atmosphere and the ocean. The ocean
120 continuously receives atmospheric forcing at every time step (30 minutes) and the
121 temperature changes accordingly, but the SST seen by the atmospheric model is fixed
122 at each timestep for a specified time span (e.g., 1, 3, 6, 12, 18, 24, and 30 days). That
123 is, the SST seen by the atmospheric model only changed until the end of the specified
124 time span.

125 Two sets of experiments in addition to the A–CTL were conducted, each
126 representing a different SST feedback frequency:

- 127 (1) High-frequency SST feedback set: This set includes the control experiment
128 (C–CTL) with SST feedback at every timestep (FF as 48/day), once a day (C–
129 1day: FF as 1/day), and every 3 days (C–3days: FF as 1/3days).
- 130 (2) Low-frequency SST feedback set: This set includes experiments with SST
131 feedback to the atmosphere for every 6 days (C–6days: FF as 1/6days), 12 days
132 (C–12days: FF as 1/12days), 18 days (C–18days: FF as 1/18days), 24 days (C–

133 24days: FF as 1/24days), and 30 days (C–30days: FF as 1/30days).

134 The SIT is coupled to CAM5 between 30° N to 30° S. The ocean was weakly
135 nudged (using a 30-day exponential time scale) between depths of 10.5 m and 107.8 m,
136 and strongly nudged (using a 1-day exponential time scale) below 107.8 m, based on
137 the climatological ocean temperature data from NCEP GODAS. No nudging was
138 applied in the upper-most 10.5 meters, allowing the simulation of rigorous air–sea
139 coupling near the ocean surface.

140 During the simulation, the SIT recalculated the SST within the tropical air–sea
141 coupling region. Outside this coupling region, the annual cycle of HadSST1 was
142 prescribed. No SST transition between the tropical air–sea coupling zone and the
143 extratropical SST-prescribed regions was applied. The ocean bathymetry for the SIT
144 was derived from the NOAA’s 1 arc-minute global relief model of Earth’s surface that
145 integrated land topography and ocean bathymetry (ETOPO1) data (Amante and Eakins,
146 2009). To ensure consistency and comparability, all observational, atmospheric, oceanic,
147 and reanalysis data were interpolated into a horizontal resolution of $1.9^\circ \times 2.5^\circ$ for
148 model initialization, nudging, and comparison of experimental simulations.

149

150 **2.3 Methodology**

151 The analysis focused on the boreal winter period (November–April), the season
152 with the most pronounced eastward propagation of the MJO. To identify intraseasonal
153 variability, the CLIVAR MJO Working Group diagnostics package (CLIVAR, 2009)
154 and a 20–100-day filter (Wang et al., 2014) was used. MJO phases were defined based
155 on the Real-time Multivariate MJO series 1 (RMM1) and series 2 (RMM2) proposed
156 by Wheeler and Hendon (2004), which utilized the first two principal components of
157 combined near-equatorial OLR and zonal winds at 850 and 200 hPa. The band-pass
158 filtered data were used to calculate the index and define the MJO phases.

159 Analysis of column-integrated MSE budgets was conducted to investigate the
 160 association between tropical convection and large-scale circulations. The column-
 161 integrated MSE budget equation (e.g., Sobel et al., 2014) is approximately given by

$$162 \left\langle \frac{\partial h}{\partial t} \right\rangle' = - \left\langle u \frac{\partial h}{\partial x} \right\rangle' - \left\langle v \frac{\partial h}{\partial y} \right\rangle' - \left\langle w \frac{\partial h}{\partial p} \right\rangle' + \langle LW \rangle' + \langle SW \rangle' + \langle SH \rangle' + \langle LH \rangle' \quad (1)$$

163 where h denotes the moist static energy

$$164 h = c_p T + gz + L_v q \quad (2)$$

165 where T is temperature (K); q is specific humidity (Kg Kg^{-1}); c_p is dry air heat capacity
 166 at constant pressure ($1004 \text{ J K}^{-1} \text{ kg}^{-1}$); L_v is latent heat of condensation (taken constant
 167 at $2.5 \times 10^6 \text{ J kg}^{-1}$); u and v are horizontal and meridional wind (m s^{-1}), respectively; w
 168 is the vertical pressure velocity (Pa s^{-1}); LW and SW are the longwave and shortwave
 169 radiation flux (W m^{-2}), respectively; and LH and SH are the latent and sensible surface
 170 heat flux (W m^{-2}), respectively. The angle bracket ($\langle * \rangle$) represents mass-weighted
 171 vertical integration from 1000 to 100 hPa; and the intraseasonal anomalies are
 172 represented as $\langle * \rangle'$.

173

174 **3. Results**

175 **3.1 The mean state and intraseasonal variability of SST**

176 The variability of SSTs plays a crucial role in the dynamics of the MJO. Studies
 177 based on observations from TOGA COARE and DYNAMO revealed that MJO events
 178 exhibited a stronger ocean temperature response compared to average conditions (de
 179 Szoeké et al., 2014). Wu et al. (2021) revealed the better MJO prediction skill in the
 180 CGCM could be contributed by the improved representation of high-frequency SST
 181 fluctuations related to the MJO, with warm (cold) SST anomalies to the east (west) of
 182 MJO convection, through the convection–SST feedback processes (Li et al., 2020a; Wu
 183 et al., 2021). It is therefore necessary to check on the influences of coupling and coupling
 184 frequency on the SST fluctuations.

185 Table 2 presents the oceanic temperature anomalies for the DJF seasonal mean,
186 including the differences in oceanic temperature between the SST and depths of 10m
187 ($\overline{\Delta T_{0-10m}}$) and 30m ($\overline{\Delta T_{0-30m}}$), as well as 20–100 days maximum and minimum SST
188 and oceanic temperature at 10m depth (T_{10m}). The region of 110–130° E and 5–15° S
189 was selected because of the largest variation in the 20–100-day bandpass-filtered SST
190 when the MJO passes over the Indo-Pacific region. Simulated DJF seasonal mean SST
191 (300.8K to 302.0 K) are generally smaller than OISST (302.2 K) but increase with the
192 lower SST feedback frequency except in C–30days (302.7 K), while the SST standard
193 deviation remains within 0.8 K, smaller than OISST (0.96 K), except in C–24days (1.06
194 K) and C–30days (1.71 K).

195 The simulated subsurface (0–10m and 0–30m) ocean temperatures were compared
196 with those in the NCEP GODAS reanalysis and presented as ($\overline{\Delta T_{0-10m}}$ and $\overline{\Delta T_{0-30m}}$).
197 The $\overline{\Delta T_{0-10m}}$ in high-frequency experiments maintained 0.1 K temperature difference.
198 In low-frequency experiments, $\overline{\Delta T_{0-10m}}$ increased from 0.2 to 1.0 K with decreasing
199 SST feedback frequency. The temperature difference ($\overline{\Delta T_{0-30m}}$) in both high-frequency
200 and low-frequency experiments remains approximately 0.8K, except for C–24days and
201 C–30days with an increase as high as 1.4 K and 2.1 K, respectively. The comparison
202 revealed the cooling effect of the SIT on the seasonal mean SST, especially in the higher-
203 frequency coupling experiment due to the more rigorous heat exchanges between ocean
204 and atmosphere. However, in the lower frequency experiments, the SST became much
205 warmer and so did vertical temperature differences due likely to the unrealistically large
206 heat accumulation of loss in the ocean.

207 As for the MJO simulation, the SST fluctuation is more relevant. The OISST
208 fluctuation through a MJO cycle was about ± 0.21 K. In comparison, the uncoupled A–
209 CTL, which was forced by monthly mean HadISST1, yielded a negligible SST
210 fluctuation (-0.003–0.02 K) as expected. In the high-frequency experiments, SST

211 fluctuated in magnitudes similar to that in the daily OISST. The amplitude became
212 unrealistically larger in the low-frequency coupling experiments with C–30days
213 reaching as high as 0.6 K. The increasingly larger amplitudes were likely resulted from
214 the heat accumulation in the ocean because of less frequent feedback (or heat release) to
215 the model atmosphere. Changes in coupling frequency led to different amplitudes of SST
216 fluctuation in a MJO cycle. As will be revealed latter, this effect had marked influence
217 on the MJO simulations.

218

219 **3.2 MJO simulation: high-frequency and low-frequency SST feedback experiments**

220 **3.2.1 General structure**

221 The propagation characteristics of the different experiments were analyzed using
222 the wavenumber-frequency spectrum (W-FS). The spectra of unfiltered U850 in ERA5,
223 A–CTL, and all coupling experiments with different feedback frequency are shown in
224 Fig. 1a–j. The C–CTL experiment accurately captures the eastward propagating signals
225 at zone wavenumber 1 with 30–80-day period (Fig. 1a and 1c), although with a slightly
226 larger amplitude than ERA5 (Fig. 1a). By contrast, the uncoupled A–CTL produced an
227 unrealistic spectral shift to time scales longer than 30–80 days (Fig. 1b) and simulated
228 the unrealistic westward propagation at wavenumber 2.

229 The W-FS spectra of the C–1day and C–3day experiment show two peaks for zone
230 wavenumber 1 over the 30 to 80-day period. The low-frequency experiments (i.e., from
231 C–6days to C–30days) increasingly enhanced the amplitudes and lowered the
232 frequency of intraseasonal perturbations with decreasing feedback frequency.
233 Furthermore, unrealistic westward W-FS of U850 becomes evident in (Fig. 1h–i) in the
234 C–18days, C–24days, and C–30days experiments, reflecting the stationary nature of
235 simulated MJO.

236 The Hovmöller diagrams in Fig. 2a–j depict the evolution of 10° N–10° S averaged
237 precipitation and U850 anomalies on intraseasonal timescales, represented by the
238 lagged correlation coefficients with the precipitation averaged over 10° S–5° N, 75–
239 100° E. In GPCP/ERA5, observed precipitation and U850 propagated eastward from
240 the eastern IO to the dateline, with precipitation leading U850 by approximately a
241 quarter of a cycle and a propagation speed of about 5 m s⁻¹ (Fig. 2a). The A–CTL
242 simulation was dominated by stationary features, with westward-propagating tendency
243 over the IO and weak and slow eastward propagation over the MC and WP (Fig. 2b).
244 The Hovmöller diagrams derived from high-frequency and low-frequency experiments
245 (Fig. 2c–h) display the key eastward propagation characteristics in both precipitation
246 and U850, as well as the phase relationship between them, except in C–24days and C–
247 30days that were dominated by stationary perturbations. Further decreased feedback
248 frequency from 1/C–24days to 1/C–30days also further weakened the signals of
249 precipitation and U850. More detailed discussion on this topic will be presented in the
250 subsequent chapter.

251 We conducted a wavenumber-frequency power spectral analysis (Wheeler and
252 Kiladis 1999) to examine the phase lag and coherence between the tropical circulation
253 and convection. Figures 3a–i illustrate the symmetric part of OLR and U850 for
254 NOAA/ERA5 data and all model experiments. The MJO band exhibits a high degree
255 of coherence, indicating a strong correlation between NOAA MJO-related OLR signal
256 and wavenumbers 1–3 (Fig. 3a). The phase lag in the 30–80-day band is approximately
257 90°, consistent with previous studies (Ren et al., 2019; Wheeler and Kiladis 1999). All
258 model experiments simulated the coherence within wavenumber 3 in the MJO band,
259 with a phase lag similar to NOAA/ERA5 data. However, the A–CTL spectrum exhibits
260 only half of the observed coherence peak at wavenumber 1, and also weaker coherence
261 at wavenumbers 2–3 for the 30–80-day period compared to NOAA/ERA5 data. The

262 experiments C-CTL, C-1day, C-3days, C-6days, C-12days, and C-18days yielded
263 wavenumber-1 coherence peak similar to that in NOAA/ERA5. Additionally, as the
264 SST feedback frequency decreases from 1/12days to 1/30days, the experiments
265 increasingly simulated unrealistic coherence in the very low frequency with a wide
266 range of zonal wavenumber from 1 to 12 (Fig. 3g-j), i.e., no zonal scale preference.

267 Figure 4 shows the phase-longitude diagrams in which the 20-100-day filtered
268 precipitation (shaded) and SST (contour) anomalies were averaged over 10° S to 10° N
269 to determine the relationship between precipitation and SST fluctuations and to provide
270 insights into the connection between air-sea coupling and convection. As expected, the
271 A-CTL did not simulate the eastward-propagating coupled SST-convection
272 perturbations as in observation (Fig. 4a), whereas C-CTL, C-1day, and C-3days
273 properly reproduced the observed features. The eastward-propagating coupled
274 perturbations were also simulated in C-6days, C-12days, and C-18days, but with
275 unrealistically increasing amplitudes near the dateline, especially in the C-18days
276 experiment. The perturbation amplification near the dateline was likely due to the lack
277 of ocean circulation in the CAM5-SIT. The amplification was also seen in C-24days
278 that failed to simulate the eastward-propagating intraseasonal perturbations. When
279 coupling frequency was reduced to 1/30days, the eastward propagation could no longer
280 be simulated and was replaced by unorganized standing oscillations in much smaller
281 zonal scales.

282 Liang et al. (2018) suggested that SST leading precipitation by 10 days implies
283 air-sea interactions at the intraseasonal timescale during MJO events, with SST playing
284 a crucial role in modulating the MJO's intensity and propagation. The A-CTL
285 simulation exhibited weak SST anomalies and stationary precipitation when using the
286 monthly average HadISST1. By contrast, the C-24days and C-30days experiment
287 showed no clear phase lag between SST and precipitation perturbations. A comparison

288 between simulation results and observation indicates that the air–sea interaction plays
289 a crucial role in facilitating eastward propagation and higher frequency feedback yields
290 more realistic simulations.

291

292 **3.2.2 Vertical structures of the MJO in the atmosphere**

293 Air–sea interaction plays a significant role in influencing atmospheric moisture and
294 convection associated with the MJO (Savarin and Chen, 2022). Whereas the ocean to
295 the east of deep convection warmed due to more downwelling shortwave radiation and
296 less heat fluxes into the atmosphere associated with weaker winds, near-surface
297 moisture convergence under the anomalous subsidence over the warmer water
298 preconditioned the eastward movement of the deep convection (DeMott et al., 2015;
299 Zhang, 2005). The MJO was noted to detour southward when crossing the MC region,
300 exhibiting enhanced convective activity preferentially in the southern MC area and
301 weaker convection in the central MC area (Hsu and Lee 2005, Wu and Hsu 2009, and
302 Kim et al. 2017). Hovmöller diagrams in Fig. 5a–j illustrate the relationship between
303 the vertical structure of air temperature (contoured, in K) and specific humidity
304 (shading, in g kg^{-1}) anomalies from the surface to 200 hPa averaged over $5\text{--}20^\circ\text{ S}$ and
305 $120\text{--}150^\circ\text{ E}$. In ERA5, the lower-level positive temperature anomaly in phase 3 (i.e.,
306 preconditioning phase) leads the development of deep temperature and moisture
307 anomalies (i.e., deep convection) after phase 4 over the MC, when moisture anomalies
308 reached the maxima at 700–500 hPa. This two-phase upward development was not
309 properly simulated in A–CTL, which shows sudden switch between positive and
310 negative anomalies in the entire troposphere, instead of progressively upward
311 development with time. The upward development was generally simulated in coupled
312 simulations from C–CTL to C–6days (Fig. 5c–e), although the negative temperature
313 anomalies below 500 hPa were over-simulated after phase 5. It became less well

314 simulated beyond C-12days and was gradually replaced by sudden phase switch as in
315 the A-CTL, especially in C-30days (Fig. 5f-j). The preconditioning phase completely
316 disappears in C-18 days and beyond. As identified in previous studies, the two-phase
317 upward development is a manifestation of air-sea coupling. The missing of this
318 coupling evidently resulted in the poor simulation in the A-CTL and extremely low
319 feedback frequency experiments.

320

321 **3.2.3 Vertical structures of the MJO in the ocean**

322 The 1-D turbulence kinetic energy (TKE) ocean model incorporates a high vertical
323 resolution that captures the vertical gradient of temperature in the upper ocean. Figure
324 6 (left column) illustrates the vertical structures of oceanic temperature between 0- and
325 60-meters during phase 2-3 when the deep convection occurred over the eastern IO
326 (60-90° E) and easterly anomalies prevailed over the MC and western Pacific. In the
327 high-frequency experiments (Fig. 6a, 6c, 6e), the upper oceanic temperatures exhibit
328 warming patterns within 30 meters depth at 100-140° E (i.e., east of the deep
329 convection and under the easterly anomalies), apparently due to more downwelling
330 short wave radiation and less heat flux release to the atmosphere. By contrast, the
331 cooling near the dateline was associated with westerly anomalies. With decreasing
332 feedback frequency, the cooling to the east of 150°E seen in high frequency experiments
333 was replaced by oceanic warming that amplified with further feedback frequency
334 decrease. The warming region that became more widespread and larger amplitude with
335 less frequent feedback eventually grew to cover the entire IO and WP, an area much
336 larger than the scale of the atmospheric MJO. The mismatch between the atmospheric
337 and oceanic anomalies suggested the weakening atmospheric-ocean coupling that
338 resulted in poor simulation of the MJO in the low frequency feedback simulations. The
339 emergence of small-scale unorganized structures with decreasing feedback frequency

340 is also evident in phase 4-5 (right column of Fig. 6), e.g., negative ocean temperature
341 anomalies in the Indian Ocean under the prevailing westerly anomalies.

342

343 **4. Discussion**

344 **4.1 Dynamic lead–lag relationship in intraseasonal variability**

345 The lead–lag relationship refers to a situation where one variable (leading) is
346 cross-correlated with the values of another variable (lagging) in subsequent phases,
347 particularly in the case of SST fluctuations and MJO-related atmospheric variations
348 between phase 1 and 8 within the domain of 110–130° E and 5–15° S (Fig. 7). The
349 analyzed variables include 20–100-day filtered latent heat flux (LHF, indicated by green
350 shading), OLR (indicated by a yellow bar chart), net surface solar radiation (FSNS,
351 indicated by an orange bar chart), U850 (indicated by a purple bar chart), 30-meter
352 depth oceanic temperature (30-m T multiplied by 100, indicated by a black line), and
353 SST (multiplied by 10, indicated by an orange line). Positive value in LHF and FSNS
354 represents an upward flux from ocean to atmosphere.

355 Decrease in LHF, which indicates a reduction in heat loss from the ocean, and
356 negative FSNS, indicating that solar radiation is heating the ocean, coincide with
357 easterly anomaly that contributes to positive SST anomaly in ERA5 (Fig. 7a). Reversed
358 fluxes are associated with westerly anomalies. This lead–lag relationship depicts the in-
359 situ atmospheric forcing on the oceanic variability during a MJO. As the MJO
360 convection progresses through the region (110–130° E and 5–15° S), several changes
361 in atmospheric and oceanic variables occur. These changes include a shift in OLR from
362 positive to negative values, a decrease in SST, a transition to westerly winds, and an
363 increase in positive FSNS and LHF (Fig. 7a). The temporal variations in SST anomaly
364 from C–CTL to C–12days were predominantly influenced by FSNS, with LHF playing
365 a secondary role, similar to the findings of Gao et al. (2020a). With the exception of

366 experiments of A-CTL, C-24days, and C-30days, both the high-frequency and low-
367 frequency SST feedback experiments simulated similar lead-lag relationships as in
368 ERA5 (Fig. 7c-h). In the C-24days and C-30days experiments, LHF was the largest
369 flux term (note the different vertical scale for the two experiments) whereas the wind,
370 OLR, and FSNS anomalies were much weaker than in other experiments. In the A-CTL
371 experiment, which was forced by monthly HasISST1 data, the SST anomalies were
372 small as expected, whereas fluxes although weak are still evident in response to
373 atmospheric perturbations (Fig. 7b). Conversely, in both C-24days and C-30days
374 experiments, a misalignment in the lead-lag relationship was observed, accompanied
375 by weak anomalies in OLR and FSNS. (Fig. 7i and 7j). This disparity between LHF and
376 wind was likely due to the unrealistically widespread and large oceanic warming as
377 shown in Fig. 6m and 6o.

378 In the simulations, the maximum positive anomaly in 30-m T was delayed by one
379 phase compared to SST, indicating the transfer of heat from the ocean surface into the
380 upper ocean progressively. Similarly, the occurrence of the most negative 30-m T
381 anomaly was also delayed by one phase compared to SST, revealing the buffering role
382 of the upper ocean when the atmospheric component of the MJO extracted (or deposited)
383 heat (energy) from (in) the ocean (Fig. 7c-i). This delayed effect was also evident in
384 the field campaign. de Szoeke et al. (2015) observed that the warmest 10-m ocean
385 temperature occurred a few days later than the peak temperature at 0.1 m. Additionally,
386 the 0.1-m ocean temperature was typically as warm as or warmer than the 10-m
387 temperature as seen in Fig. 6. In the extreme low frequency feedback experiments, the
388 amplitude of 30-m temperature became unrealistically large due likely to the continuous
389 accumulation or loss of the ocean heat.

390

391 **4.2 Unorganized perturbations in extreme frequency feedback scenarios**

392 DeMott et al. (2014) noted that in uncoupled experiments, the NCAR CAM
393 superparameterized version 3 (SPCAM3) exhibited strong eastward propagation when
394 5-day running mean SST was prescribed, but relatively weaker propagation for monthly
395 mean SST. This raises the question of how much SST feedback periodicity is necessary
396 to maintain robust eastward propagation in coupled experiments. This tendency was
397 also seen in our study, that is, slower propagation (or weaker tendency) with decreased
398 feedback frequency until the C-24days experiment (Figs. 1-7). By 1/30days, the
399 perturbations became stationary.

400 Generally, C-18days exhibited the unrealistic overestimation of intraseasonal
401 variability while maintaining eastward propagation of the MJO. Here, we are not
402 suggesting that C-18days represents the optimal SST feedback experiment. Figure 8
403 highlights the considerable differences in the simulation of MJO perturbations at phase
404 2-3 in C-18days and C-30days experiments. In C-18days, negative OLR anomalies
405 were widespread from the western Indian Ocean to the MC, while in reality it should
406 be observed mainly in the Indian Ocean and be accompanied by positive anomalies in
407 the eastern MC, i.e., a west-east dipolar structure (Fig. 8a). In C-30days, the OLR
408 anomaly, although was still the dominant feature in the Indian Ocean-western Pacific
409 region, became much weaker and characterized by smaller scale perturbations. These
410 OLR anomalies were generally associated with upper-level convergence (not shown)
411 embedded in much weaker wind anomalies (U200) compared to those in C-18days.
412 The circulation and OLR in C-24days exhibited the characteristics similar to those in
413 C-18days but with the OLR anomalies breaking up into smaller scales.

414 Furthermore, in the C-18days and C-24days experiments, positive anomalies in
415 LHF and net surface heat flux (Fig. 8d, 8e, 8g, and 8h) were predominantly observed
416 in the convection-inactive region to the east of 150°E where low-level easterly wind
417 and negative SST anomalies prevailed (Fig. 8j). The OLR, winds, heat fluxes, and SST

418 to the west of 150°E exhibited similar correspondences between variables but in
419 opposite phase. With feedback frequency reduced to 1/30days (Fig. 8f, 8i, and 8l), the
420 heat fluxes and SST anomalies broke into unorganized smaller scale features,
421 consistent with the ocean temperature shown in Fig. 6h. Although the wind fields in the
422 both upper and lower levels were still characterized by large-scale structure, the
423 corresponding divergence were dominated by much smaller scale perturbations (not
424 shown), similar to heat fluxes and SST. The increasingly dominant smaller scale
425 perturbations can also be inferred from Fig. 2h-j and 4h-j. In addition, the large power
426 spectra in the low frequency band spread across a wide range of wavenumbers,
427 reflecting the smaller scale nature of the simulated perturbations in C-30days (Fig. 3h-
428 j). This disparity between the scale of rotational and divergent winds suggests that the
429 poor coupling between the convection and large-scale circulation.

430 With decreased feedback frequency of SST from C-CTL to C-30days, the ocean
431 continued to receive atmospheric forcing, but the feedback response was delayed,
432 leading to the accumulation or loss of energy (temperature) in the upper ocean, as seen
433 in the SST distribution in the WP (Fig. 6 and 8). Subsequently, the C-30days
434 experiment exhibited comprehensive disorder over the Indo-Pacific region, with the
435 SST exhibiting a perturbed unrealistically spatial distribution (Fig. 8l) associated with
436 plus-minus latent heat flux and 10m wind anomalies (Fig. 8f), net surface heat flux, and
437 solar radiation (Fig. 8i). As a result, the organized large-scale circulation seen in the
438 MJO was not manifested. To this extreme, the air-sea interaction observed in the MJO
439 no longer worked properly in the model.

440

441 **4.3 Moist static energy (MSE) budget analysis**

442 We diagnosed the relative contribution of each term in Eq. (1) to the MSE tendency
443 with a focus on the second (pre-conditioning) and fifth (convection crossing the MC)

444 phases. Figure 9 illustrates the physical processes associated with each term (averaged
445 over 10°S – 0° , 120 – 150°E) contributing to the column-integrated MSE tendency
446 ($\langle \text{dmdt} \rangle$) in Eq. (1) during phase 2 in ERA5 and model simulations. In ERA5, when
447 the MJO convection was in the eastern Indian Ocean, the column-integrated vertical
448 and horizontal advection ($-\langle \text{wdmdp} \rangle$ and $-\langle \text{vdm} \rangle$) over the MC area were the dominant
449 terms in the MSE budget and largely compensated by longwave radiation and latent
450 heat flux, as reported in Wang and Li (2020) and Tseng et al. (2022). All experiments
451 simulated the positive and negative contributions similar to those derived from ERA5
452 although with different amplitudes. Notably, the C–24days and C–30days simulated
453 relatively weak vertical advection and too strong negative latent heat flux and too weak
454 longwave radiation flux. As a result, the C–24days and C–30days simulated relatively
455 weak tendency compared to other experiments. The results are consistent with the poor
456 simulation of the MJO in the extreme low frequency feedback experiments discussed
457 above.

458 We compared the spatial distribution of column-integrated MSE tendency $\langle \text{dmdt} \rangle$
459 (shading), precipitation (contours), and 850-hPa wind (vectors) during phase 5, i.e., the
460 period when the strongest convection crossing the MC (Fig. 10). In ERA5, the main
461 convection (indicated by positive precipitation anomaly) is accompanied by low-level
462 convergence in the 850-hPa wind across the MC extending into the WP (Fig. 10a). A
463 positive $\langle \text{dmdt} \rangle$ is observed to the east of the MJO convection to the south of the
464 equator (Fig. 10a). Conversely, a negative tendency is observed to the west of the MJO
465 convection accompanied by negative precipitation anomalies further to the west. The
466 phase relationship between the MSE tendency and precipitation reflects the eastward-
467 propagating nature of the MJO. With the exception of A–CTL, C–24days, and C–
468 30days, the model simulations displayed a similar structure in the 20–100-day filtered
469 $\langle \text{dmdt} \rangle$, precipitation, and 850-hPa wind vectors (Fig. 10c–h). although the exact

470 locations may be shifted compared to those derived from ERA5. The C-CTL simulated
471 relatively weak signals compared to ERA5, whereas the signals became increasingly
472 stronger with decreasing feedback frequency. The signals became unrealistically strong
473 beyond 1/18days feedback frequency and the lead-lag relationship between the MSE
474 tendency and precipitation became less clear. For example, positive precipitation
475 anomaly became in phase with the tendency in the western Pacific south of the equator
476 in C-24days and C-30days experiments, and the tendency was much weaker in C-
477 30days. The results were consistent with the weaker eastward propagation tendency in
478 the low-frequency feedback experiments, especially in C-24days and C-30days when
479 the feedback frequency became unrealistically low.

480 The corresponding MSE budget during phase 5 is shown in Fig. 10. The MC
481 has been identified as a barrier to the eastward propagation of the MJO (Hsu and Lee,
482 2005, Wu and Hsu 2009, Tseng et al. 2017, Li et al., 2020b) and approximately 30–50%
483 of the MJO experienced stalling over the MC (Zhang and Han, 2020). To determine
484 whether the MJO has sufficient energy to traverse the MC, we focused the analysis on
485 phase 5. Figure 11 illustrates the projection of each MSE component and decomposition
486 of the horizontal MSE advection at phase 5 over the MC region (20° S– 20° N, 90° –
487 210° E) following the approach of Tseng et al. (2022) and Jiang et al. (2018), where
488 F_s is total surface fluxes including SH and LH, and Q_r is vertically integrated net SW
489 and LW radiation. Unlike in phase 2 when vertical advection is the dominant term, the
490 MSE tendency was dominated by the horizontal MSE advection $\langle vdm \rangle$ in ERA5 and
491 all experiments, except the A-CTL. This contribution increased with decreasing SST
492 feedback frequency. The weaker positive vertical advection $\langle wmdp \rangle$ did not vary
493 systematically with decreasing feedback frequency and even turned negative in C-
494 24days and C-30days. F_s and Q_r acted to damp the tendency by cancelling out the
495 effect of the advection term. F_s tended to be more negative with decreasing feedback

496 frequency and became much larger in C–30days. By contrast, Q_r was unrealistically
497 weak in C–18days, C–24days, and C–30days. The uncoupled simulation yielded much
498 weaker amplitude in all terms as expected.

499 The $\langle v_{dm} \rangle$ that contributed most to the eastward propagation of the MJO in
500 phase 5 was further decomposed into zonal ($\langle u_{dmx} \rangle$) and meridional ($\langle v_{dm} \rangle$)
501 components to examine their relative effects (Fig. 11). Both components contributed
502 positively, but the $\langle v_{dm} \rangle$ exhibited a larger amplitude, consistent with Tseng et al.
503 (2014, 2022). The $\langle v_{dm} \rangle$ of high-frequency SST feedback experiments yielded
504 results closely similar to ERA5. Comparatively, the $\langle v_{dm} \rangle$ term in low-frequency
505 SST feedback experiments (C–18days, C–24days, and C–30days) became
506 unrealistically large with decreasing feedback frequency.

507 Spatial distributions of $\langle w_{dmp} \rangle$, $\langle v_{dm} \rangle$, and 200-hPa wind at phase 5 are
508 shown in Fig. 12. In ERA5, the wind divergence at 200 hPa at phase 5 (Fig. 12a),
509 overlaid the 850-hPa convergence (Fig. 10a), reflecting a deep convection structure.
510 The model simulations exhibited a similar structure to ERA5 except in A–CTL, C–
511 24days, and C–30days experiments, and again the amplitude increased with decreasing
512 feedback frequency. In ERA5, negative $\langle w_{dmp} \rangle$ and $\langle v_{dm} \rangle$ anomalies (Fig. 12a)
513 were observed to the west of the MJO convection (Fig. 10a). The spatial distribution of
514 the negative $\langle v_{dm} \rangle$ anomaly (dashed-red contours) extends from the IO to the MC
515 and positive anomaly (predominantly meridional advection from the south, not shown)
516 in the western-central Pacific south of the equator tends to facilitate the eastward
517 propagation of deep convection in the western Pacific, consistent with Tseng et al.
518 (2014, 2022). The $\langle w_{dmp} \rangle$ with negative and positive anomaly to the west and east
519 of the deep convection also contributes to the eastward propagation of the MJO, but
520 with weaker contribution than $\langle v_{dm} \rangle$. Again, these characteristics were not simulated
521 in A-CTL, whereas the amplitudes of both terms became increasingly larger with

522 decreasing feedback frequency until becoming unrealistically large beyond 1/18days.
523 In C–30days experiment both terms exhibited unorganized spatial structure as shown
524 in preceding discussion. In summary, the high-frequency feedback experiments
525 simulated an approximately 80% projection of $\langle vdm \rangle$ in ERA5, whereas the low-
526 frequency SST feedback experiments overestimated $\langle vdm \rangle$ anomalies (Fig. 12f–h).

527

528 **5. Conclusions**

529 This study built upon the work of Lan et al. (2022) and Tseng et al. (2022) by
530 coupling a high-resolution 1-D TKE ocean model (the SIT model) with the CAM5, i.e.,
531 a CAM5–SIT configuration, to investigate the effects of intraseasonal SST feedback on
532 the MJO. We introduced asymmetric exchange frequencies between the atmosphere and
533 the ocean, ensuring bidirectional interaction at each timestep within the experimental
534 periodicity by fixing the SST value in the coupler. This allowed us to create SST
535 feedback with various intervals at 30 minutes, 1, 3, 6, 12, 18, 24, and 30 days.

536 The aim is to assess the effect of SST feedback frequency, namely, how often
537 should the atmosphere-driven SST change feedback to the atmosphere and whether
538 there is a limit. With the exception of the C–24days and C–30days experiment, both the
539 high-frequency and low-frequency experiments demonstrated realistic simulations of
540 various aspects of the MJO when compared to ERA5, GPCP, and OISST data, although
541 the simulation results becoming increasingly amplified and unrealistic with decreasing
542 feedback frequency. These aspects included intraseasonal periodicity (Fig. 1), eastward
543 propagation (Fig. 2 and 4), coherence in the intraseasonal band (Fig. 3), tilting vertical
544 structure (Fig. 5), intraseasonal SST (Table 2) and oceanic temperature variances (Fig.
545 6), the lead–lag relationship of intraseasonal variability (Fig. 7), contribution of each
546 term to the column-integrated MSE tendency at the preconditioning phase (phase 2)
547 and mature phased (phase 5) (Fig. 9 and Fig. 11). The MSE tendency term was

548 dominated by the horizontal and vertical MSE advection in phase 5 and phase 2,
549 respectively, in ERA5 and most experiments. Furthermore, we deliberately extended
550 the SST feedback interval to an unrealistically long 30 days to investigate the limits of
551 delayed ocean response. The main conclusion is less frequent the update, more
552 unrealistic the simulation result.

553 The lead-lag relationship provides a visual representation of the variations in 20-
554 100-day filtered LHF, FSNS, OLR, U850 and SST with positive SST anomaly leading
555 the onset of the MJO convection (Fig. 7). This relationship highlights the
556 interconnected nature of surface heat fluxes, solar radiation, and atmospheric
557 circulation patterns, underscoring their mutual influence and interplay through air-sea
558 interaction. Our results indicate that the high-frequency (low-frequency) SST
559 experiments tended to underestimate (overestimate) the MJO simulation in CAM5-SIT
560 model. Whether this finding can be applied to other models warrants further
561 investigations.

562 The result of C-3days experiment is consistent with Stan (2018), suggesting the
563 absence of 1-5-day variability in SST would promote the amplification of westward
564 power associated with tropical Rossby waves. By comparing with the control
565 experiment in which SST feedback occurs at every time step (30 minutes), the C-1day
566 experiment (SST feedback once daily) confirmed the findings of Hagos et al. (2016)
567 and Lan et al. (2022) that the removal of the diurnal cycle would enhance the MJO. The
568 increasing feedback periodicity of SST in low-frequency experiments led to the
569 accumulation of atmospheric influences through short-wave and long-wave radiations
570 and surface heat fluxes, resulting in an unrealistically large ocean temperature
571 anomalies and variances within few tens of meters below ocean surface (Table 2). The
572 large-scale nature of the MJO remains intact with decreasing feedback frequency,
573 although becoming increasingly unrealistic in both structure and amplitude, until

574 1/30days when the intraseasonal fluctuations were overwhelmingly dominated by
575 unorganized small scale perturbations in both atmosphere and ocean, as well as at the
576 atmosphere-ocean interface where heat and energy were rigorously exchanged.

577 The reason causing the sudden change between C-24days and C-30days is not
578 entirely clear. Two possibilities are discussed here. The first possible reason leading to
579 this disorder is that when the ocean feedback is delayed for as long as 30 days (more
580 than half of the MJO period) both positive and negative fluxes would contribute to the
581 heat accumulation or loss in the ocean because of the MJO phase transition and result
582 in unorganized small scale structures in ocean temperatures, which could in turn affect
583 the heat flux and convection. The second would be the SST change become more abrupt
584 and disrupt the large-scale nature of the MJO. However, whether large-amplitude SST
585 fluctuations would induce unorganized small-scale perturbation is debatable. As seen
586 in many hypothetic (or theoretical) studies, a sudden initiation of SST (or step-function
587 like) could induce large scale responses. This issue remains an open question that
588 warrants further studies with purposely designed experiment to untangle.

589 Finally, results of intraseasonal SST feedback experiments on MJO are
590 summarized schematically in Fig. 13, following DeMott et al. (2014). These
591 experiments included the uncoupled experiment (A-CTL), high-frequency SST
592 experiments (C-CTL, C-1day, and C-3days), low-frequency SST experiments (C-
593 6days, C-12days, C-18days), and extreme low-frequency experiment (C-24days and
594 C-30days). In the absence of intraseasonal SST variability, the eastward propagation of
595 the MJO was disrupted, leading to weakened or fragmented MJO activity as shown in
596 Fig. 13a. On the other hand, the high-frequency SST experiments closely mimicked
597 air-sea interaction and well captured the characteristics of the MJO. The time-varying
598 SSTs in the coupled simulation provided a certain degree of organization and sufficient
599 surface fluxes, which facilitated the development of the MJO circulation as illustrated

600 in Fig. 13b. The horizontal moist static energy tendency derived from increased low-
601 level convergence, especially due to the meridional advection of MSE, intensified the
602 MJO convection and triggered the eastward propagation over the MC region. The PBL
603 convergence ahead of the MJO convection is due to Kelvin-wave dynamics (Jiang,
604 2017), in conjunction with the background zonal flow structure (Tulich and Kiladis,
605 2021). Horizontal MSE or moisture advection in the lower troposphere, particularly the
606 seasonal mean low-level MSE influenced by the MJO's anomalous winds, has had a
607 significant impact on the MJO propagation. (Gonzalez and Jiang, 2017; Jiang, 2017).
608 This simulation result is consistent with the understanding that the MJO is primarily
609 attributed to the interaction between organized convection and large-scale circulations
610 that triggers the eastward propagation. As feedback frequency become lower, the major
611 characteristics of the MJO could still be simulated as depicted in Fig. 13c, but with
612 overestimated amplitudes and deteriorating simulations in spatial structures. In the
613 extreme low frequency experiments with frequency decreasing to 1/24days and
614 1/30days, unorganized structures started to emerge and broke up into smaller scale
615 perturbations as shown in Fig. 13d, when proper air–sea interaction did not operate
616 properly in the model. Eventually in the C–30days experiment, unrealistically and
617 spatially scattered anomalies in precipitation, SST, surface heat fluxes, and vertical and
618 horizontal MSE advection became dominant features. All these findings led to the
619 major conclusion of this study: spontaneous atmosphere-ocean interaction with high
620 resolution ocean model is a key to the proper simulation of the MJO in the climate
621 models.

622

623 *Code and data availability.* The model code of CAM5–SIT is available at
624 <https://doi.org/10.5281/zenodo.5510795>. Input data of CAM5–SIT using the
625 climatological Hadley Centre Sea Ice and Sea Surface Temperature dataset and

626 GODAS data forcing, including 30-year numerical experiments, are available at
627 <https://doi.org/10.5281/zenodo.5510795>.

628

629 *Author contributions.* YYL is the CAM5–SIT model developer and writes the majority
630 part of the paper. HHH contributes to the physical explanation and the reorganization
631 and revision of the manuscript. WLT assists in the MSE analysis.

632

633 *Competing interests.* The authors declare that they have no conflict of interest.

634

635 *Acknowledgements.* The contribution from YYL, HHH, and WLT to this study is
636 supported by the Ministry of Science and Technology of Taiwan under MOST 110-
637 2123-M-001-003, MOST 110-2811-M-001-603, MOST 109-2811-M-001-624 and
638 MOST108-2811-M-001-643. Our deepest gratitude goes to the editors and anonymous
639 reviewers for their careful work and thoughtful suggestions that have helped improve
640 this paper substantially. We sincerely thank the National Center for Atmospheric
641 Research and their Atmosphere Model Working Group (AMWG) for release
642 CESM1.2.2. We thank the computational support from National Center for High
643 performance Computing of Taiwan. Thanks, ChatGPT for correcting the English
644 grammar.

645

646 **Reference**

647 Adler, R. F., Huffman, G. J., Chang, A., Ferraro, R., Xie, P.
648 P., Janowiak, J., Rudolf, B., Schneider, U., Curtis, S., Bolvin,
649 D., Gruber, A., Susskind, J., Arkin, P., and Nelkini, E.: The Version
650 2.1 Global Precipitation Climatology Project (GPCP) Monthly
651 Precipitation Analysis (1979 -Present), *J. Hydrometeor.*, 4(6), 1147-
652 1167, [https://doi.org/10.1175/1525-
653 7541\(2003\)004<1147:TVGPCP>2.0.CO;2](https://doi.org/10.1175/1525-7541(2003)004<1147:TVGPCP>2.0.CO;2), 2003.

654 Amante, C., and Eakins, B. W.: ETOPO1 1 arc-minute globe relief model:
655 Procedures, data sources and analysis, NOAA Tech. Memo. NESDIS

- 656 NGDC-24, NOAA, Silver Spring, MD, 19 pp.,
657 <https://doi.org/10.7289/V5C8276M>, 2009.
- 658 Banzon, V. F., Reynolds, R. W., Stokes, D., and Xue, Y.: A 1/4-spatial-
659 resolution daily sea surface temperature climatology based on a
660 blended satellite and in situ analysis, *J. Climate*, 27, 8221–8228,
661 <https://doi.org/10.1175/JCLI-D-14-00293.1>, 2014.
- 662 Behringer, D. W., and Xue, Y.: Evaluation of the global ocean data
663 assimilation system at NCEP: The Pacific Ocean. Eighth Symposium
664 on Integrated Observing and Assimilation Systems for Atmosphere,
665 Oceans, and Land Surface, AMS 84th Annual Meeting, Washington
666 State Convention and Trade Center, Seattle, Washington, 11-15.
667 Derber, J.C., and A. Rosati, 1989: A global oceanic data assimilation
668 system, *J. Phys. Oceanogr.*, 19, 1333–1347,
669 <https://ams.confex.com/ams/pdfpapers/70720.pdf>, 2004.
- 670 Chang, M.-Y., Li, T., Lin, P.-L., and Chang, T.-H.: Forecasts of MJO
671 Events during DYNAMO with a Coupled Atmosphere-Ocean Model:
672 Sensitivity to Cumulus Parameterization Scheme, *J. Meteorol.*
673 *Res.*, 33, 1016–1030, <https://doi.org/10.1007/s13351-019-9062-5>,
674 2019.
- 675 CLIVAR MADDEN–JULIAN OSCILLATION WORKING GROUP: MJO
676 simulation diagnostics, *J. Climate*, 22, 3006–3030,
677 <https://doi.org/10.1175/2008JCLI2731.1>, 2009.
- 678 DeMott, C. A., Klingaman, N. P., and Woolnough, S. J.: Atmosphere-
679 ocean coupled processes in the Madden-Julian oscillation, *Rev. of*
680 *Geophysics*, 53, 1099– 1154, <https://doi.org/10.1002/2014RG000478>,
681 2015.
- 682 DeMott, C. A., Stan, C., Randall, D. A., and Branson, M.
683 D.: Intraseasonal variability in coupled GCMs: The roles of ocean
684 feedbacks and model physics, *J.*
685 *Climate*, 27(13), 4970– 4995. [https://doi.org/10.1175/JCLI-D-13-](https://doi.org/10.1175/JCLI-D-13-00760.1)
686 [00760.1.](https://doi.org/10.1175/JCLI-D-13-00760.1), 2014.
- 687 de Szoek, S. P., Edson, J. B., Marion, J. R., Fairall, C. W., and Bariteau,
688 L.: The MJO and air–sea interaction in TOGA COARE and
689 DYNAMO, *J.*
690 *Climate*, 28(2), 597– 622. [https://doi.org/10.1175/JCLI-D-14-](https://doi.org/10.1175/JCLI-D-14-00477.1)
691 [00477.1](https://doi.org/10.1175/JCLI-D-14-00477.1), 2014.
- 692 de Szoek, S. P., Edson, J. B., Marion, J. R., Fairall, C. W., and Bariteau,
693 L.: The MJO and air–sea interaction in TOGA COARE and
694 DYNAMO, *J. Climate*, 28, 597–622, [https://doi.org/10.1175/JCLI-](https://doi.org/10.1175/JCLI-D-14-00477.1)
695 [D-14-00477.1](https://doi.org/10.1175/JCLI-D-14-00477.1), 2015.
- 696 de Szoek, S. P., and Maloney, E.: Atmospheric mixed layer
697 convergence from observed MJO sea surface temperature
698 anomalies, *J.*
699 *Climate*, 33(2), 547– 558. <https://doi.org/10.1175/JCLI-D-19->

- 700 0351.1, 2020.
- 701 Fu, J. X., Wang, W., Shinoda, T., Ren, H. L., and Jia, X.: Toward
702 understanding the diverse impacts of air–sea interactions on MJO
703 simulations, *J. Geophys. Res.-*
704 *Oceans*, 122(11), 8855– 8875. [https://doi.org/10.1002/2017JC01318](https://doi.org/10.1002/2017JC013187)
705 7, 2017.
- 706 Gao, Y., Hsu, P.-C., Chen, L., Wang, L., and Li, T.: Effects of high-
707 frequency surface wind on the intraseasonal SST associated with the
708 Madden-Julian oscillation, *Clim. Dynam.*, 54, 4485–4498,
709 <https://doi.org/10.1007/s00382-020-05239-w>, 2020a.
- 710 Gao, Y., Klingaman, N. P., DeMott, C. A., and Hsu, P.-C.: Boreal
711 summer intraseasonal oscillation in a superparameterized general
712 circulation model: effects of air–sea coupling and ocean mean state,
713 *Geosci. Model Dev.*, 13, 5191–5209, [https://doi.org/10.5194/gmd-](https://doi.org/10.5194/gmd-13-5191-2020)
714 13-5191-2020, 2020b.
- 715 Ge, X., Wang, W., Kumar, A., and Zhang, Y.: Importance of the vertical
716 resolution in simulating SST diurnal and intraseasonal variability in
717 an oceanic general circulation model, *J. Climate*, 30, 3963–
718 3978, <https://doi.org/10.1175/JCLI-D-16-0689.1>, 2017.
- 719 Gonzalez, A. O., and Jiang, X.: Winter mean lower tropospheric moisture
720 over the maritime continent as a climate model diagnostic metric for
721 the propagation of the Madden-Julian Oscillation, *Geophys. Res.*
722 *Lett.*, 44(5), 2588–2596. <https://doi.org/10.1002/2016GL072430>,
723 2017.
- 724 Hagos, S. M., Zhang, C., Feng, Z., Burleyson, C. D., Mott, C. De, Kerns,
725 B., Benedict, J. J., and Martini, M. N.: The impact of the diurnal
726 cycle on the propagation of Madden-Julian Oscillation convection
727 across the Maritime Continent, *J. Adv. Model. Earth Syst.*, 8, 1552–
728 1564, <https://doi.org/10.1002/2016MS000725>, 2016.
- 729 Hersbach, H., and Dee, D.: ERA5 reanalysis is in production, ECMWF
730 Newsletter, Vol. 147, p.
731 7, [https://www.ecmwf.int/en/newsletter/147/news/era5-reanalysis-](https://www.ecmwf.int/en/newsletter/147/news/era5-reanalysis-production)
732 [production](https://www.ecmwf.int/en/newsletter/147/news/era5-reanalysis-production), 2016.
- 733 Hong, X., Reynolds, C. A., Doyle, J. D., May, P., and O'Neill, L.:
734 Assessment of upper-ocean variability and the Madden-Julian
735 Oscillation in extended-range air–ocean coupled mesoscale
736 simulations, *Dyn. Atmos. Oceans*, 78, 89–105.
737 <https://doi.org/10.1016/j.dynatmoce.2017.03.002>, 2017.
- 738 Hsu, H.-H., and Lee, M.-Y.: Topographic effects on the eastward
739 propagation and initiation of the Madden-Julian Oscillation, *J.*
740 *Climate*, 18, 795-809, <https://doi.org/10.1175/JCLI-3292.1>, 2005.
- 741 Hurrell, J. W., Holland, M. M., Gent, P. R., Ghan, S., Kay, J. E., Kushner,
742 P. J., Lamarque, J.-F., Large, W. G., Lawrence, D., Lindsay, K.,
743 Lipscomb, W. H., Long, M. C., Mahowald, N., Marsh, D. R., Neale,

- 744 R. B., Rasch, P., Vavrus, S., Vertenstein, M., Bader, D., Collins, W.
745 D., Hack, J. J., Kiehl, J., and Marshall, S.: The Community Earth
746 System Model: A framework for collaborative research, *Bull. Amer.*
747 *Meteor. Soc.*, 94, 1339–1360, [https://doi.org/10.1175/BAMS-D-12-](https://doi.org/10.1175/BAMS-D-12-00121.1)
748 00121.1, 2013.
- 749 Jiang, X., Waliser, D. E., Xavier, P. K., Petch, J., Klingaman, N. P.,
750 Woolnough, S. J., Guan, B., Bellon, G., Crueger, T., DeMott, C.,
751 Hannay, C., Lin, H., Hu, W., Kim, D., Lappen, C.-L., Lu, M.-M.,
752 Ma, H.-Y., Miyakawa, T., Ridout, J. A., Schu-bert, S. D., Scinocca,
753 J., Seo, K.-H., Shindo, E., Song, X., Stan, C., Tseng, W.-L., Wang,
754 W., Wu, T., Wu, X., Wyser, K., Zhang, G. J., and Zhu, H.: Vertical
755 structure and physical processes of the Madden-Julian oscillation:
756 Exploring key model physics in climate simulations, *J. Geophys.*
757 *Res.-Atmos.*, 120, 4718–4748,
758 <https://doi.org/10.1002/2014JD022375>, 2015.
- 759 Jiang, X.: Key processes for the eastward propagation of the Madden-
760 Julian Oscillation based on multimodel simulations, *J. Geophys. Res.*
761 *Atmos.*, 122, 755–770, <https://doi.org/10.1002/2016JD025955>, 2017.
- 762 Jiang, X., Adames, Á. F., Zhao, M., Waliser, D., and Maloney, E.: A
763 unified moisture mode framework for seasonality of the Madden-
764 Julian oscillation, *J. Climate*, 31, 4215–4224,
765 <https://doi.org/10.1175/JCLI-D-17-0671.1>, 2018.
- 766 Jiang, X., Adames, Á. F., Kim, D., Maloney, E. D., Lin, H., and Kim, H.,
767 Zhang, C., DeMott, C. A., and Klingaman, N. P.: Fifty years of
768 research on the Madden-Julian Oscillation: Recent progress,
769 challenges, and perspectives, *J. Geophys. Res.-Atmos.*, 125,
770 e2019JD030911, <https://doi.org/10.1029/2019JD030911>, 2020.
- 771 Kim, D., Kim, H., and Lee, M.-I.: Why does the MJO detour the Maritime
772 continent during Austral summer? *Geophys. Res. Lett.*, 44(5), 2579–
773 2587, <https://doi.org/10.1002/2017gl072643>, 2017.
- 774 Kim, H., Vitart, F., and Waliser, D. E.: Prediction of the Madden-Julian
775 oscillation: A review, *J. Climate*, 31(23), 9425–9443,
776 <https://doi.org/10.1175/JCLI-D-18-0210.1>, 2018.
- 777 Klingaman, N. P., and Demott, C. A.: Mean state biases and interannual
778 variability affect perceived sensitivities of the Madden-Julian
779 oscillation to air–sea coupling, *J. Adv. Model. Earth Syst.*, 12, 1–22,
780 <https://doi.org/10.1029/2019MS001799>, 2020.
- 781 Krishnamurti, T. N., Oosterhof, D. K. and Mehta, A. V.: Air–sea
782 interaction on the time scale of 30 to 50 days, *J. Atmos. Sci.*, 45,
783 1304–1322, [https://doi.org/10.1175/1520-](https://doi.org/10.1175/1520-0469(1988)045,1304:AIOTTS.2.0.CO;2)
784 0469(1988)045,1304:AIOTTS.2.0.CO;2, 1988.
- 785 Lambaerts, J., Lapeyre, G., Plougonven, R., and Klein, P.: Atmospheric
786 response to sea surface temperature mesoscale structures, *J.*
787 *Geophys. Res.-Atmos.*, 118(17), 9611–9621.

- 788 <https://doi.org/10.1002/jgrd.50769>, 2020.
- 789 Lan, Y.-Y., Hsu, H.-H., Tseng, W.-L., and Jiang, L.-C.: Embedding a
790 one-column ocean model in the Community Atmosphere Model 5.3
791 to improve Madden–Julian Oscillation simulation in boreal winter,
792 *Geosci. Model Dev.*, 15, 5689–5712, [https://doi.org/10.5194/gmd-](https://doi.org/10.5194/gmd-15-5689-2022)
793 [15-5689-2022](https://doi.org/10.5194/gmd-15-5689-2022), 2022.
- 794 Li, Y., Han, W., Shinoda, T., Wang, C., Ravichandran, M., and Wang,
795 J.-W.: Revisiting the wintertime intraseasonal SST variability in the
796 tropical south Indian Ocean: Impact of the ocean interannual
797 variation, *J. Phys. Oceanogr.*, 44, 1886–1907,
798 <https://doi.org/10.1175/JPO-D-13-0238.1>, 2014.
- 799 Li, T., Ling, J., and Hsu, P.-C.: Madden–Julian Oscillation: Its discovery,
800 dynamics, and impact on East Asia, *J. Meteor. Res.*, 34, 20–42,
801 <https://doi.org/10.1007/s13351-020-9153-3>, 2020a.
- 802 Li, K., Yu, W., Yang, Y., Feng, L., Liu, S., and Li, L.: Spring barrier to
803 the MJO eastward propagation, *Geophys. Res. Lett.*, 47, e2020GL087788, <https://doi.org/10.1029/2020GL087788>,
804 <https://doi.org/10.1029/2020GL087788>,
805 2020b.
- 806 Liang, Y.; Du, Y.; Zhang, L.; Zheng, X.; Qiu, S. The 30–50-Day
807 Intraseasonal Oscillation of SST and Precipitation in the South
808 Tropical Indian Ocean, *Atmos.*, 9, 69.
809 <https://doi.org/10.3390/atmos9020069>, 2018.
- 810 Liang, Y., and Du, Y.: Oceanic impacts on 50–80-day intraseasonal
811 oscillation in the eastern tropical Indian Ocean, *Clim. Dynam.*, 59,
812 1283–1296, <https://doi.org/10.1007/s00382-021-06041-y>, 2022.
- 813 Liebmann, B.: Description of a complete (interpolated) outgoing
814 longwave radiation dataset, *B. Am. Meteorol. Soc.*, 77, 1275–1277,
815 1996.
- 816 Madden, R. A., and Julian, P. R.: Description of global-scale circulation
817 cells in the tropics with a 40-50 day period, *J. Atmos. Sci.*, 29, 1109-
818 1123, [https://doi.org/10.1175/1520-](https://doi.org/10.1175/1520-0469(1972)029<1109:DOGSCC>2.0.CO;2)
819 [0469\(1972\)029<1109:DOGSCC>2.0.CO;2](https://doi.org/10.1175/1520-0469(1972)029<1109:DOGSCC>2.0.CO;2), 1972.
- 820 Maloney, E., and Sobel, A. H.: Surface fluxes and ocean coupling in the
821 tropical intraseasonal oscillation. *J. Climate*, 17, 4368–4386,
822 <https://doi.org/10.1175/JCLI-3212.1>, 2004.
- 823 Newman, M., Sardeshmukh, P. D., and Penland, C.: How important is
824 air–sea coupling in ENSO and MJO evolution? *J. Climate*, 22, 2958– 2977, <https://doi.org/10.1175/2008JCLI2659.1>,
825 <https://doi.org/10.1175/2008JCLI2659.1>,
826 2009.
- 827 Pariyar, S.K., Keenlyside, N., Tseng, W.-L., Hsu, H.-H., and Tsuang, B.-
828 J. The role of air–sea coupling on November–April intraseasonal
829 rainfall variability over the South Pacific, *Clim. Dynam.*, 60, 1121–
830 1136, <https://doi.org/10.1007/s00382-022-06354-6>, 2023.

- 831 Pei, S., Shinoda, T., Soloviev, A., and Lien, R.-C.: Upper ocean response
832 to the atmospheric cold pools associated with the Madden-Julian
833 Oscillation, *Geophys. Res. Lett.*, 45, 5020–5029,
834 <https://doi.org/10.1029/2018GL077825>, 2018.
- 835 Rasch, P. J., Xie, S., Ma, P.-L., Lin, W., Wang, H., Tang, Q., Bur-
836 rows, S. M., Caldwell, P., Zhang, K., Easter, R. C., Cameron-
837 Smith, P., Singh, B., Wan, H., Golaz, J.-C., Harrop, B. E., Roesler, E.,
838 Bacmeister, J., Larson, V. E., Evans, K. J., Qian, Y., Taylor, M.,
839 Leung, L. R., Zhang, Y., Brent, L., Branstet-
840 ter, M., Hannay, C., Mahajan, S., Mametjanov, A., Neale, R., Richter, J. H., Yoon, J.-H.,
841 Zender, C. S., Bader, D., Flan-
842 ner, M., Foucar, J. G., Jacob, R.,
843 Keen, N., Klein, S. A., Liu, X., Salinger, A. G., Shrivastava, M., and
844 Yang, Y.: An overview of the atmospheric component of the Energy
845 Exascale Earth System Model, *J. Adv. Model Earth Sy.*, 11, 2377–
2411, <https://doi.org/10.1029/2019ms001629>, 2019.
- 846 Rayner, N. A., Parker, D. E., Horton, E. B., Folland, C. K., Alexander,
847 L. V., Rowell, D. P., Kent, E. C., and Kaplan, A.: Global analyses
848 of sea surface temperature, sea ice, and night marine air temperature
849 since the late nineteenth century, *J. Geophys. Res.*, 108(D14), 4407,
850 <https://doi.org/10.1029/2002JD002670>, 2003.
- 851 Ren, P. F., Gao, L., Ren, H.-L., Rong, X., and Li, J.: Representation of
852 the Madden–Julian Oscillation in CAMSCSM, *J. Meteor. Res.*, 33,
853 627–650, <https://doi.org/10.1007/s13351-019-8118-x>, 2019.
- 854 Savarin, A., and Chen, S. S.: Pathways to better prediction of the MJO:
855 2. Impacts of atmosphere-ocean coupling on the upper ocean and
856 MJO propagation, *J. Adv. Model. Earth Syst.*, 14, e2021MS002929,
857 <https://doi.org/10.1029/2021MS002929>, 2022.
- 858 Shinoda, T., Pei, S., Wang, W., Fu, J. X., Lien, R.-C., Seo, H.,
859 and Soloviev, A.: Climate process team: Improvement of ocean
860 component of NOAA climate forecast system relevant to Madden-
861 Julian Oscillation simulations, *J. Adv. Model. Earth Syst.*, 13(12),
862 e2021MS002658. <https://doi.org/10.1029/2021MS002658>, 2021.
- 863 Seo, H., Subramanian, A. C., Miller, A. J., and Cavanaugh, N.
864 R.: Coupled impacts of the diurnal cycle of sea surface temperature
865 on the Madden–Julian oscillation, *J.*
866 *Climate*, 27(22), 8422– 8443. [https://doi.org/10.1175/JCLI-D-14-
867 00141.1](https://doi.org/10.1175/JCLI-D-14-00141.1), 2014.
- 868 Sobel, A. H., and Gildor, H.: A simple time-dependent model of SST hot
869 spots. *J. Climate*, 16, 3978–3992, [https://doi.org/10.1175/1520-
870 0442\(2003\)016<3978:ASTMOS>2.0.CO;2](https://doi.org/10.1175/1520-0442(2003)016<3978:ASTMOS>2.0.CO;2), 2003.
- 871 Sobel, A. H., Maloney, E. D., Bellon, G., and Frierson, D. M.: Surface
872 Fluxes and Tropical Intraseasonal Variability: a Reassessment, *J.*
873 *Adv. Model. Earth Syst.*, 2, 2,
874 <https://doi.org/10.3894/JAMES.2010.2.2>, 2010.

- 875 Sobel, A., Wang, S., and Kim, D.: Moist static energy budget of the MJO
876 during DYNAMO, *J. Atmos. Sci.*, 71(11), 4276– 4291,
877 <https://doi.org/10.1175/JAS-D-14-0052.1>, 2014.
- 878 Stan, C.: The role of SST variability in the simulation of the MJO, *Clim.*
879 *Dynam.*, 51, 2943–2964, [https://doi.org/10.1007/s00382-017-4058-](https://doi.org/10.1007/s00382-017-4058-2)
880 2, 2018.
- 881 Tseng, W.-L., Tsuang, B.-J., Keenlyside, N. S., Hsu, H.-H. and Tu, C.-
882 Y.: Resolving the upper-ocean warm layer improves the simulation
883 of the Madden-Julian oscillation, *Clim. Dynam.*, 44, 1487–1503,
884 <https://doi.org/10.1007/s00382-014-2315-1>, 2015.
- 885 Tseng, W.-L., Hsu, H.-H., Keenlyside, N., Chang, C.-W. J., Tsuang, B.-
886 J., Tu, C.-Y., and Jiang, L.-C.: Effects of Orography and Land–Sea
887 Contrast on the Madden–Julian Oscillation in the Maritime
888 Continent: A Numerical Study Using ECHAM-SIT, *J. Climate*, 30,
889 9725–9741, <https://doi.org/10.1175/JCLI-D-17-0051.1>, 2017.
- 890 Tseng, W.-L., Hsu, H.-H., Lan, Y.-Y., Lee, W.-L., Tu, C.-Y., Kuo, P.-
891 H., Tsuang, B.-J., and Liang, H.-C.: Improving Madden–Julian
892 oscillation simulation in atmospheric general circulation models by
893 coupling with a one-dimensional snow–ice–thermocline ocean
894 model, *Geosci. Model Dev.*, 15, 5529–5546,
895 <https://doi.org/10.5194/gmd-15-5529-2022>, 2022.
- 896 Tulich, S. N., and Kiladis, G. N.: On the Regionality of moist kelvin
897 waves and the MJO: The critical role of the background zonal flow,
898 *J. Adv. Model. Earth Syst.*, 13(9), e2021MS002528.
899 <https://doi.org/10.1029/2021MS002528>, 2021.
- 900 Voldoire, A., Roehrig, R., Giordani, H., Waldman, R., Zhang, Y., Xie,
901 S., and Bouin, M.-N.: Assessment of the sea surface temperature
902 diurnal cycle in CNRM-CM6-1 based on its 1D coupled
903 configuration, *Geosci. Model Dev.*, 15, 3347–3370,
904 <https://doi.org/10.5194/gmd-15-3347-2022>, 2022.
- 905 Wang, W., Hung, M.-P., Weaver, S. J., Kumar, A., and Fu, X.: MJO
906 prediction in the NCEP Climate Forecast System version 2, *Clim.*
907 *Dynam.*, 42, 2509–2520, [https://doi.org/10.1007/s00382-013-1806-](https://doi.org/10.1007/s00382-013-1806-9)
908 9, 2014.
- 909 Wang, L. and Li, T.: Effect of vertical moist static energy advection on
910 MJO eastward propagation: Sensitivity to analysis domain, *Clim.*
911 *Dynam.*, 54, 2029–2039, [https://doi.org/10.1007/s00382-019-](https://doi.org/10.1007/s00382-019-05101-8)
912 05101-8, 2020.
- 913 Watterson, I. G.: The sensitivity of subannual and intraseasonal tropical
914 variability to model ocean mixed layer depth, *J. Geophys. Res.*, 107,
915 4020, <https://doi.org/10.1029/2001JD000671>, 2002.
- 916 Wheeler, M. C., and Hendon, H. H.: An all-season real-time multivariate
917 MJO index: development of an index for monitoring and prediction,
918 *Mon. Weather Rev.*, 132, 1917–1932, <https://doi.org/10.1175/1520->

- 919 0493(2004)132<1917:AARMMI>2.0.CO;2, 2004.
- 920 Wheeler, M., and Kiladis, G. N.: Convectively coupled equatorial waves:
921 Analysis of clouds and temperature in the wavenumber-frequency
922 domain, *J. Atmos. Sci.*, 56, 374– 399, [https://doi.org/10.1175/1520-0469\(1999\)056<0374:CCEWAO>2.0.CO;2](https://doi.org/10.1175/1520-0469(1999)056<0374:CCEWAO>2.0.CO;2), 1999.
- 924 Wu, C.-H., and Hsu, H.-H.: Potential Influence of Topography on the
925 MJO in the Maritime Continent, *J. Climate*, 22, 5433-5448,
926 <https://doi.org/10.1175/2009JCLI2825.1>, 1999.
- 927 Wu, J., Li, Y., Luo, J.-J. and Jiang, X.: Assessing the role of air–sea
928 coupling in predicting Madden–Julian oscillation with an
929 Atmosphere–Ocean coupled model, *J. Clim.* 34 9647–63,
930 <https://doi.org/10.1175/JCLI-D-20-0989.1>, 2021.
- 931 Zhang, L., and Han, W.: Barrier for the eastward propagation of
932 Madden–Julian Oscillation over the maritime continent: A possible
933 new mechanism, *Geophys. Res. Lett.*, 47(21),
934 e2020GL090211. <https://doi.org/10.1029/2020gl090211>, 2020.
- 935 Zhao, N., and Nasuno, T.: How Does the Air–Sea Coupling Frequency
936 Affect Convection During the MJO Passage?, *J. Adv. Model. Earth
937 Sy.*, 12, e2020MS002058, <https://doi.org/10.1029/2020MS002058>,
938 2020.

939 Table 1. Two sets of experiments with different SST feedback
 940 frequencies: high-frequency (C-CTL, C-1day and C-3days) and low-
 941 frequency (C-6days, C-12days, C-18days, C-24days and C-30days).

942

subseasonal sets	high-frequency SST (< 6 days)			low-frequency SST (6-30 days)				
experiments	C-CTL	C-1day	C-3days	C-6days	C-12days	C-18days	C-24days	C-30days
atmosphere to ocean frequency	48/1day							
ocean to atmosphere Frequency	48/1day	1/1day	1/3days	1/6days	1/12days	1/18days	1/24days	1/30days

943

944 Table 2. Key intraseasonal (20–100-day bandpass filtered) ocean temperatures in all
945 experiments: SST, differences between SST and temperatures at 10m depth ($\overline{\Delta T}_{0-10m}$)
946 and 30m depth ($\overline{\Delta T}_{0-30m}$), t max/mini SST and 10m-depth temperature (T_{10m}) in the
947 area of (110–130° E, 5–15° S) during a MJO cycle for the observation (OISST), AGCM
948 (A–CTL), high-frequency experiments (C–CTL, C–1day, and C–3days), and low-
949 frequency experiments (C–6days, C–12days, C–18days, C–24days, and C–30days)
950

(110–130° E, 5–15° S)		obs.	AGC M	high-frequency			low-frequency				
experiments		OI	A– CTL ²	C– CTL	C– 1day	C– 3days	C– 6days	C– 12days	C– 18days	C– 24days	C– 30days
	DJF seasonal mean	SST	302.2 ±0.96	302.2 ±0.77	300.8 ±0.76	301.2 ±0.76	301.2 ±0.75	301.2 ±0.75	301.4 ±0.75	301.6 ±0.80	302.0 ±1.06
$\overline{\Delta T}_{0-10m}$		-	-	0.1 ± 0.22	0.1 ± 0.22	0.1 ± 0.21	0.1 ± 0.23	0.2 ± 0.25	0.3 ± 0.32	0.5 ± 0.50	1.0 ± 0.95
$\overline{\Delta T}_{0-30m}$		-	-	0.8 ± 0.79	0.7 ± 0.70	0.6 ± 0.69	0.8 ± 0.70	0.8 ± 0.70	1.0 ± 0.73	1.4 ± 0.96	2.1 ± 1.54
phase's mean in boreal winter	max (phase) SST	0.21 (ph2)	0.02 (ph2)	0.24 (ph3)	0.26 (ph3)	0.22 (ph3)	0.32 (ph3)	0.36 (ph3)	0.43 (ph3)	0.50 (ph3)	0.62 (ph2)
	max T_{10m} (phase)	-	-	0.15 (ph4)	0.17 (ph4)	0.14 (ph3)	0.19 (ph3)	0.21 (ph3)	0.26 (ph3)	0.30 (ph3)	0.35 (ph2)
	mini (phase) SST	-0.21 (ph7)	-0.003 (ph8)	-0.17 (ph7)	-0.22 (ph7)	-0.19 (ph7)	-0.25 (ph7)	-0.28 (ph7)	-0.38 (ph7)	-0.52 (ph6)	-0.60 (ph6)
	mini T_{10m} (phase)	-	-	-0.11 (ph8)	-0.12 (ph7)	-0.11 (ph8)	-0.15 (ph7)	-0.17 (ph7)	-0.24 (ph7)	-0.33 (ph6)	-0.33 (ph6)

951 Note: ¹daily average data, ² monthly average data.

952 **Figure List**

953 **Figure 1.** Wavenumber–frequency spectra for 850-hPa zonal wind averaged over 10°
954 S – $10^\circ N$ in boreal winter after removing the climatological mean seasonal cycle.
955 Vertical dashed lines represent periods at 80 and 30 days. (a)–(j) are from ERA5
956 reanalysis, A–CTL, C–CTL, C–1day, C–3days, C–6days, C–12days, C–18days, C–
957 24days, and C–30days, respectively.

958

959 **Figure 2.** Hovmöller diagrams of correlation between precipitation averaged over 10°
960 S – $5^\circ N$, 75 – $100^\circ E$ and precipitation (color) and 850-hPa zonal wind (contour)
961 averaged over $10^\circ N$ – $10^\circ S$. (a)–(j) are arranged in the same order as in Fig. 1 for
962 GPCP/ERA5 and all experiments. All data are 20–100-day bandpass filtered.

963

964 **Figure 3.** Zonal wavenumber–frequency power spectra of anomalous OLR (colors) and
965 phase lag with U850 (vectors) for the symmetric component of tropical waves, with the
966 vertically upward vector representing a phase lag of 0° and phase lag increasing
967 clockwise. Three dispersion straight lines with increasing slopes representing the
968 equatorial Kelvin waves (derived from the shallow water equations) corresponding to
969 three equivalent depths, 12, 25, and 50 m, respectively. (a)–(j) are arranged in the same
970 order as in Fig. 1 for NOAA/ERA5 and all experiments.

971

972 **Figure 4.** Phase-longitude Hovmöller diagrams of 20–100-day filtered precipitation
973 (mm day^{-1} , shaded) and SST anomaly (K, contour) averaged over $10^\circ N$ – $10^\circ S$ from
974 phase 1 to 8. Contour interval is 0.03; solid, dashed, and thick-black lines represent
975 positive, negative, and zero values, respectively. (a)–(j) are arranged in the same order
976 as in Fig. 1 for NOAA/ERA5 and all experiments.

977

978 **Figure 5.** Phase-vertical Hovmöller diagrams of 20–100-day specific humidity
979 (shading, g kg^{-1}) and air temperature (contoured, K) averaged over 5 – $20^\circ S$, 120 – 150°
980 E ; solid, dashed, and thick-black curves are positive, negative, and zero values,
981 respectively. (a)–(j) are arranged in the same order as in Fig. 1 for NOAA/ERA5 and
982 all experiments.

983

984 **Figure 6.** The 20–100-day filtered oceanic temperature (K, shaded and contour,
985 interval 0.03) at phase 2–3 (Left column) and phase 4–5 (Right column) averaged
986 over 0 – $15^\circ S$ between 0 and 60 m depth. (a)–(b) are from C–CTL, (c)–(d) are from
987 C–1day, (e)–(f) are from C–3days, (g)–(h) are from C–6days, (i)–(j) are from C–
988 12days, (k)–(l) are from C–18days, (m)–(n) are from C–24days, and (o)–(p) are from
989 C–30days.

990

991 **Figure 7.** The lead–lag relationship between MJO-related atmosphere and SST
992 variation from phase 1 to 8 averaged within 110–130° E and 5–15° S. The variables
993 analyzed include 20–100-day filtered LHF, green shading), OLR (yellow bar chart),
994 FSNS, (orange bar chart), U850 (purple bar chart), 30-m T (multiplied by 100, black
995 line), and SST (multiplied by 10, orange line). Variables denoted with L (R) are scaled
996 by the left (right) y-axis. (a)–(j) are from ERA5/OISST reanalysis, A–CTL, C–CTL, C–
997 1day, C–3days, C–6days, C–12days, C–18days, C–24days, and C–30days, respectively.
998

999 **Figure 8.** Averaged 20–100-day filtered fields at phase 2–3. (Upper row) OLR (W m^{-2} ,
1000 shaded) and 200 hPa zonal and meridional wind anomaly (m s^{-1} , vector with reference
1001 vector shown at the top right corner, latent heat flux (W m^{-2} , shaded, positive
1002 representing upward), and 10-m wind anomaly (m s^{-1} , contour interval 0.5). (Second
1003 row) net surface heat flux (W m^{-2} , shaded) and net solar radiation (W m^{-2} , contour
1004 interval 6). (Third row) SST (K, shaded) and 850 hPa zonal and meridional wind
1005 anomaly (m s^{-1} , vector with reference vector shown at the top right corner. The number
1006 of days used to generate the composite is shown at the bottom right corner. (a), (d), (g)
1007 and (j) are from C–18days; (b), (e), (h) and (k) are from C–24days, and (c), (f), (i) and
1008 (l) are from C–30days, respectively. Solid, dashed, and thick-black lines represent
1009 positive, negative, and zero values, respectively.
1010

1011 **Figure 9.** Averaged 20–100-day filtered column-integrated MSE budget terms
1012 ($\text{J kg}^{-1} \text{s}^{-1}$) in 10° S–0° N/S, 120–150° E for ERA5 and all model simulations. Colors
1013 represent different datasets: green for REA5, light gray for A–CTL, red, orange and
1014 wathet blue for high-frequency experiments (C–CTL, C–1day, and C–3days,
1015 respectively), purple, black, dark brown, dark green, and dark gray for low-frequency
1016 experiments (C–6days, C–12days, C–18days, C–24days, and C–30days, respectively).
1017 The bars from left to right represent MSE tendency ($\langle \text{dmdt} \rangle$), vertical MSE advection
1018 ($-\langle \text{wdmdp} \rangle$), horizontal MSE advection ($-\langle \text{vdm} \rangle$), surface latent heat flux (LH),
1019 surface sensible heat flux (SH), shortwave radiation flux ($\langle \text{SW} \rangle$), longwave radiation
1020 flux ($\langle \text{LW} \rangle$), and residual terms.
1021

1022 **Figure 10.** Filtered the column-integrated MSE tendency ($\text{J kg}^{-1} \text{s}^{-1}$, shading),
1023 precipitation (mm d^{-1} , contours interval 1.5) and 850-hPa wind (green vector, reference
1024 vector 2 m s^{-1}) in phase 5: (a) ERA5, (b) A–CTL, (c) C–CTL, (d) C–1day, (e) C–3days,
1025 (f) C–6days, (g) C–12days, (h) C–18days, (i) C–24days, and (i) C–30days. Solid-red,
1026 dashed-blue, and thick-black curves represent positive, negative, and zero values,
1027 respectively.

1028

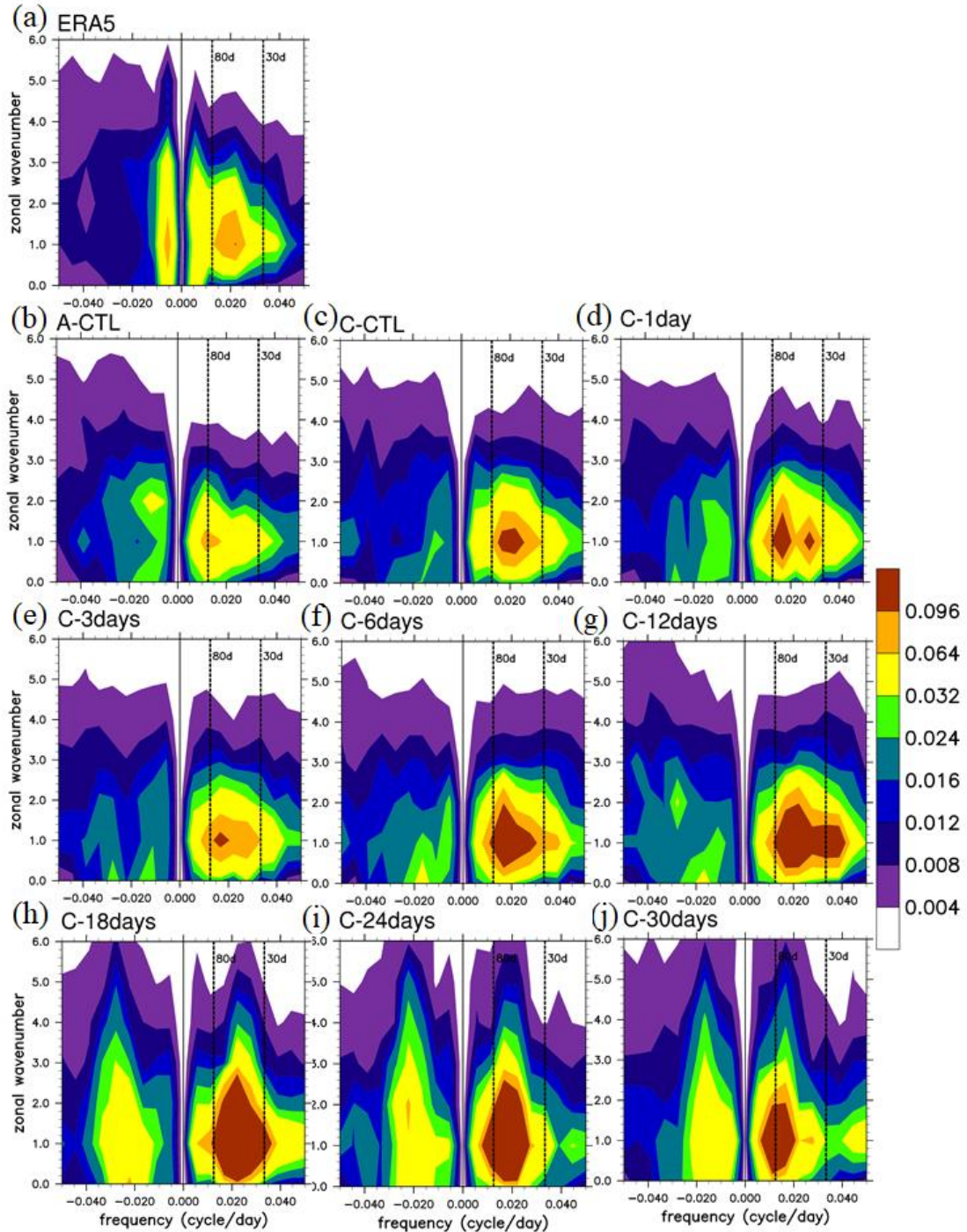
1029 **Figure 11.** The projection of each MSE component onto the ERA5 column-integrated
1030 MSE tendency at phase 5 over the MC (20° S–20° N, 90–210° E): $\langle dmdt \rangle$, $\langle wmdp \rangle$,
1031 $\langle vdm \rangle$, Q_r , F_s , and residual; decomposition of horizontal MSE advection to zonal and
1032 meridional advection ($\langle udmdt \rangle$ and $\langle vdmdy \rangle$).

1033

1034 **Figure 12.** Filtered column-integrated vertical ($\text{J kg}^{-1} \text{s}^{-1}$, shading) and horizontal MSE
1035 advection ($\text{J kg}^{-1} \text{s}^{-1}$, contours interval 6.0), and 200-hPa wind (green vector with
1036 reference vector 3 m s^{-1}): (a) ERA5, (b) A-CTL, (c) C-CTL, (d) C-1day, (e) C-3days,
1037 (f) C-6days, (g) C-12days, (h) C-18days, (i) C-24days, and (j) C-30days. Solid-blue,
1038 dashed-red, and thick-black curves represent positive, negative, and zero values,
1039 respectively.

1040

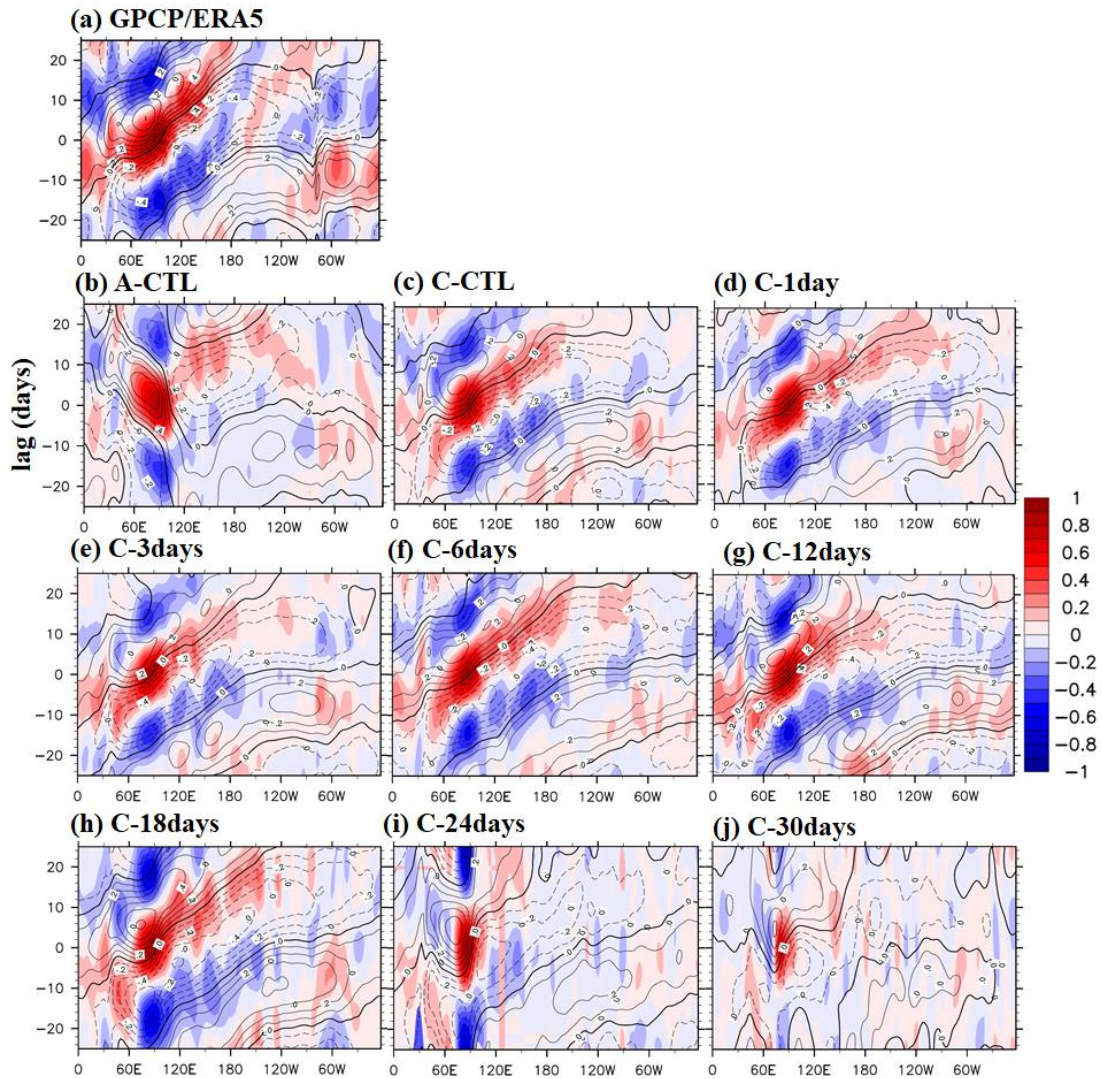
1041 **Figure 13.** Schematic diagrams illustrate the anomalous circulation and moistening
1042 processes during the eastward propagation of the MJO in experiments: (a) A-CTL, (b)
1043 high-frequency SST feedback experiments (C-CTL, C-1day, and C-3days), (c) low-
1044 frequency SST feedback experiments (C-6days, C-12days, and C-18days), and (d)
1045 C-24days and C-30days experiment. In each panel, the horizontal line represents the
1046 equator. The size of clustering gray clouds indicates the strength of convective
1047 organization. A red ellipse indicates convection-driven circulation. In the coupled
1048 simulations, light red (blue) filled ovals represent warm (cold) SST anomalies,
1049 respectively, and grass green filled rectangle represent latent heat flux. Unresolved
1050 convective processes are indicated by black dots representing low-level moisture
1051 convergence. Low-level moisture convergence into the equatorial trough is shown by
1052 light blue arrows, while midlevel moisture advection is represented by left-pointing
1053 green arrows. The deeper colors or thicker lines on the map indicate stronger anomalies
1054 of the MJO perturbations. Note: The concept of the figure is based on DeMott et al.
1055 (2014).



1056

1057 **Figure 1.** Wavenumber–frequency spectra for 850-hPa zonal wind averaged over 10°
 1058 S – 10° N in boreal winter after removing the climatological mean seasonal cycle.
 1059 Vertical dashed lines represent periods at 80 and 30 days. (a)–(j) are from ERA5
 1060 reanalysis, A-CTL, C-CTL, C-1day, C-3days, C-6days, C-12days, C-18days, C-
 1061 24days, and C-30days, respectively.

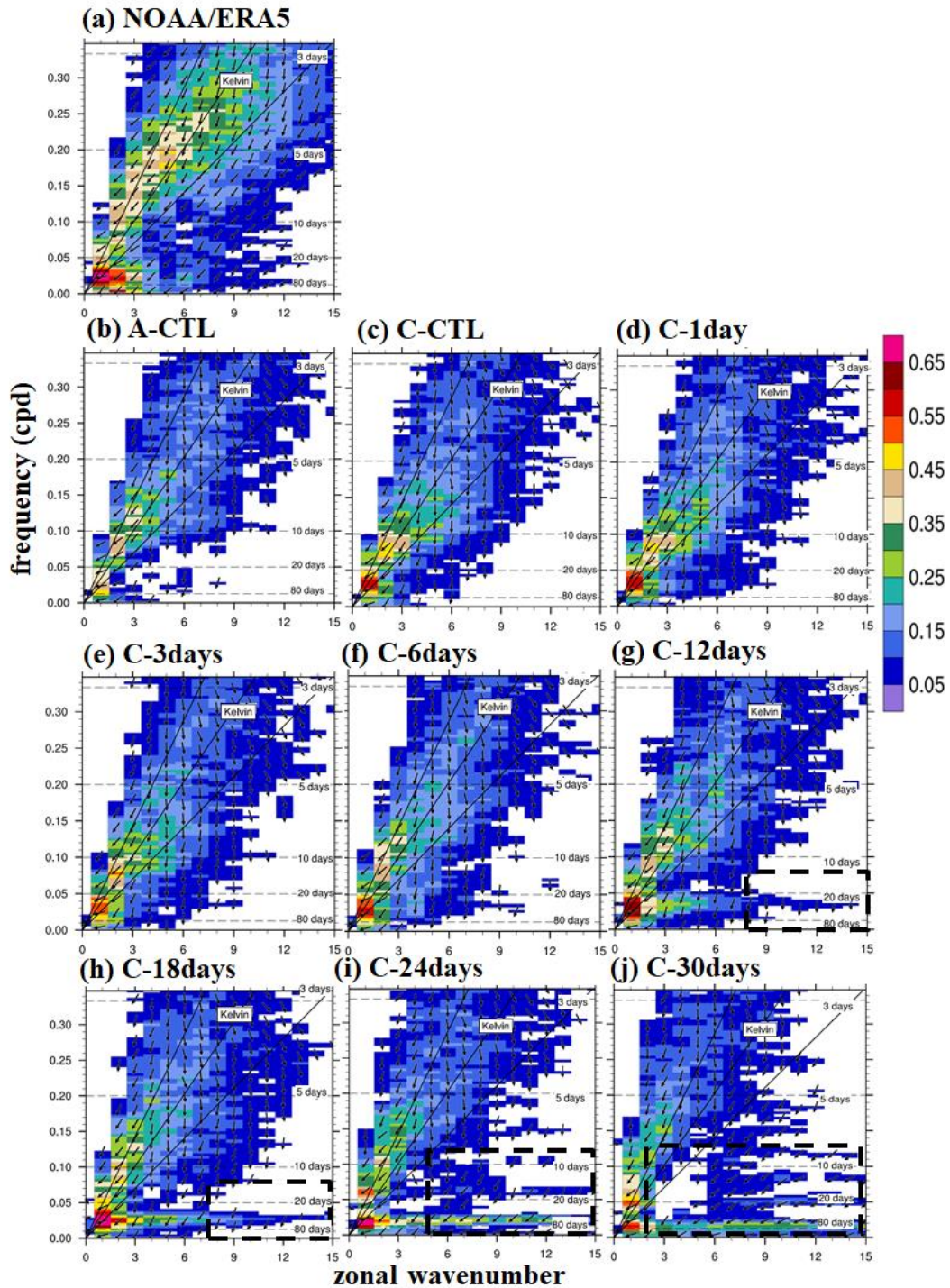
1062



1063

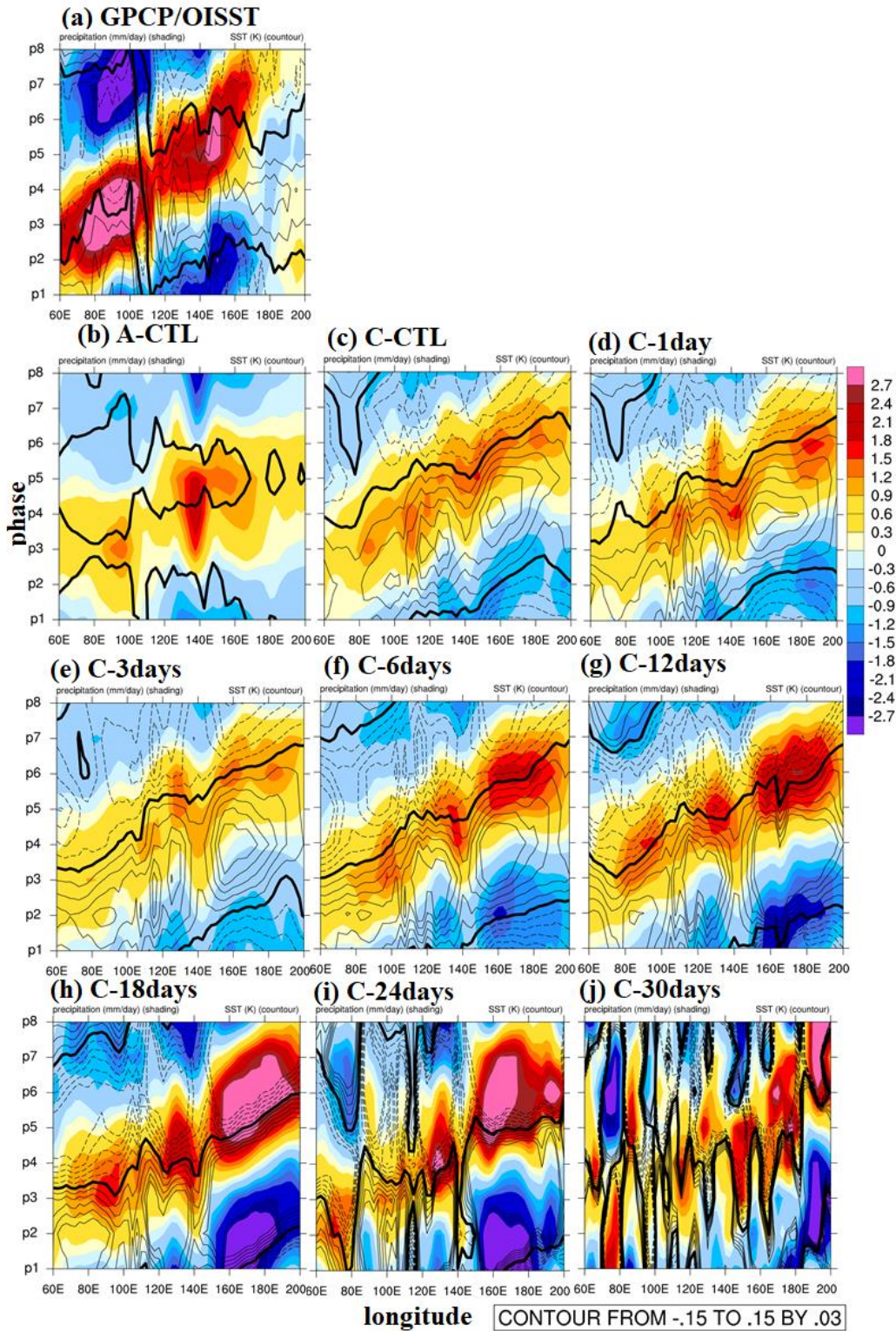
1064 **Figure 2.** Hovmöller diagrams of correlation between precipitation averaged over 10°
 1065 $S-5^{\circ} N$, $75-100^{\circ} E$ and precipitation (color) and 850-hPa zonal wind (contour)
 1066 averaged over $10^{\circ} N-10^{\circ} S$. (a)–(j) are arranged in the same order as in Fig. 1 for
 1067 GPCP/ERA5 and all experiments. All data are 20–100-day bandpass filtered.

1068



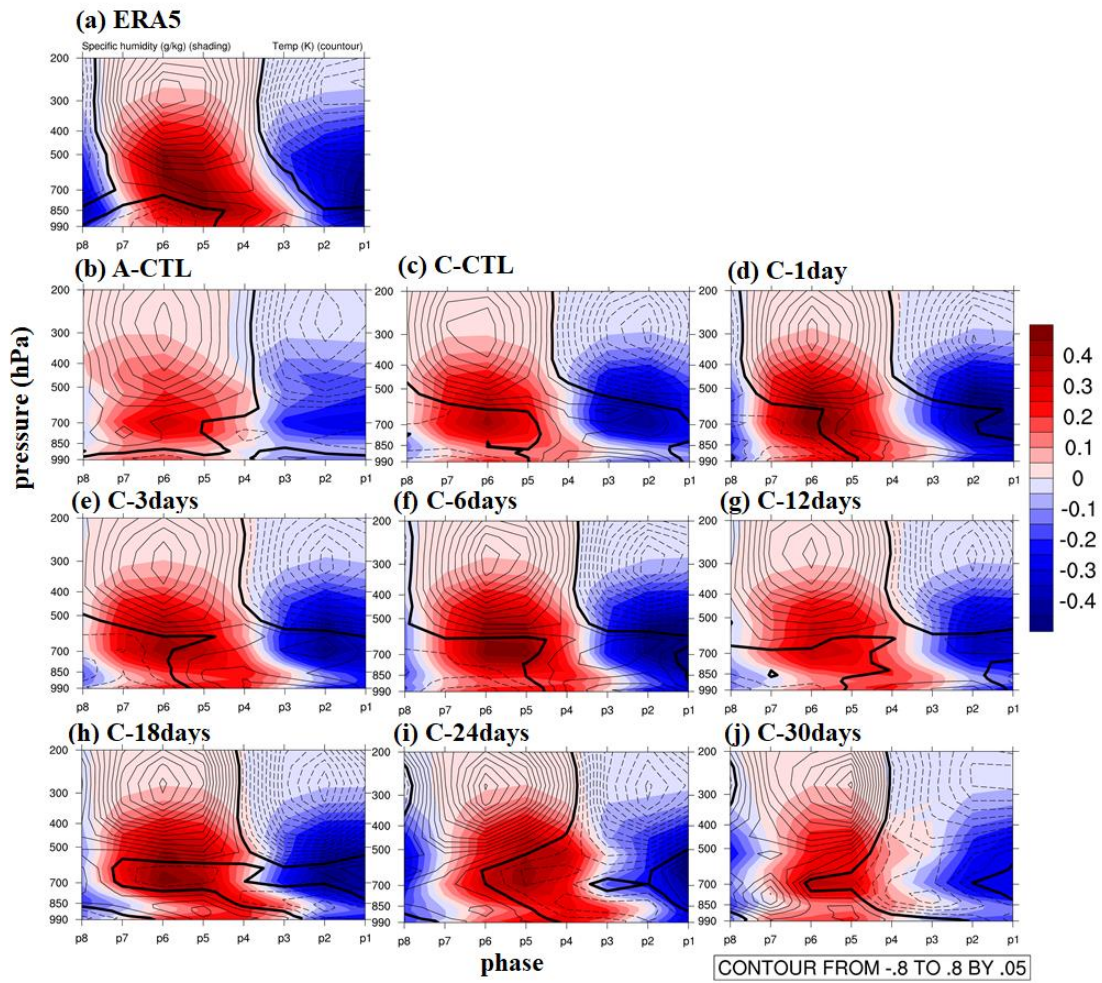
1069

1070 **Figure 3.** Zonal wavenumber–frequency power spectra of anomalous OLR (colors) and
 1071 phase lag with U850 (vectors) for the symmetric component of tropical waves, with the
 1072 vertically upward vector representing a phase lag of 0° with phase lag increasing
 1073 clockwise. Three dispersion straight lines with increasing slopes represent the
 1074 equatorial Kelvin waves (derived from the shallow water equations) corresponding to
 1075 three equivalent depths, 12, 25, and 50 m, respectively. (a)–(j) arrange in order are same
 1076 order as in Fig. 1 for NOAA/ERA5 and all experiments.



1077

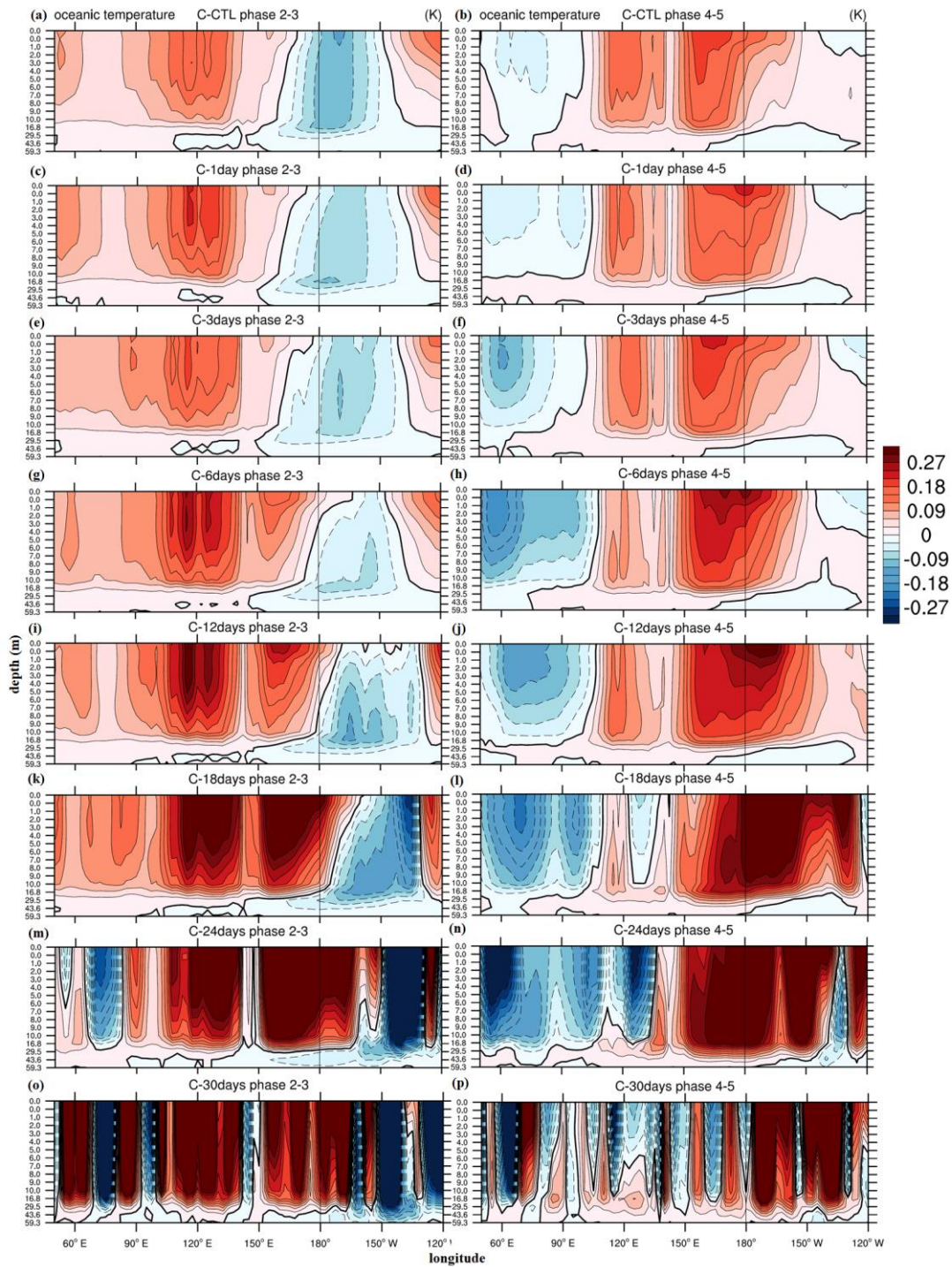
1078 **Figure 4.** Phase-longitude Hovmöller diagrams of 20–100-day filtered precipitation
 1079 (mm day⁻¹, shaded) and SST anomaly (K, contour) averaged over 10° N–10° S from
 1080 phase 1 to 8. Contour interval is 0.03; solid, dashed, and thick-black lines represent
 1081 positive, negative, and zero values, respectively. (a)–(j) are arranged in the same order
 1082 as in Fig. 1 for NOAA/ERA5 and all experiments.



1084

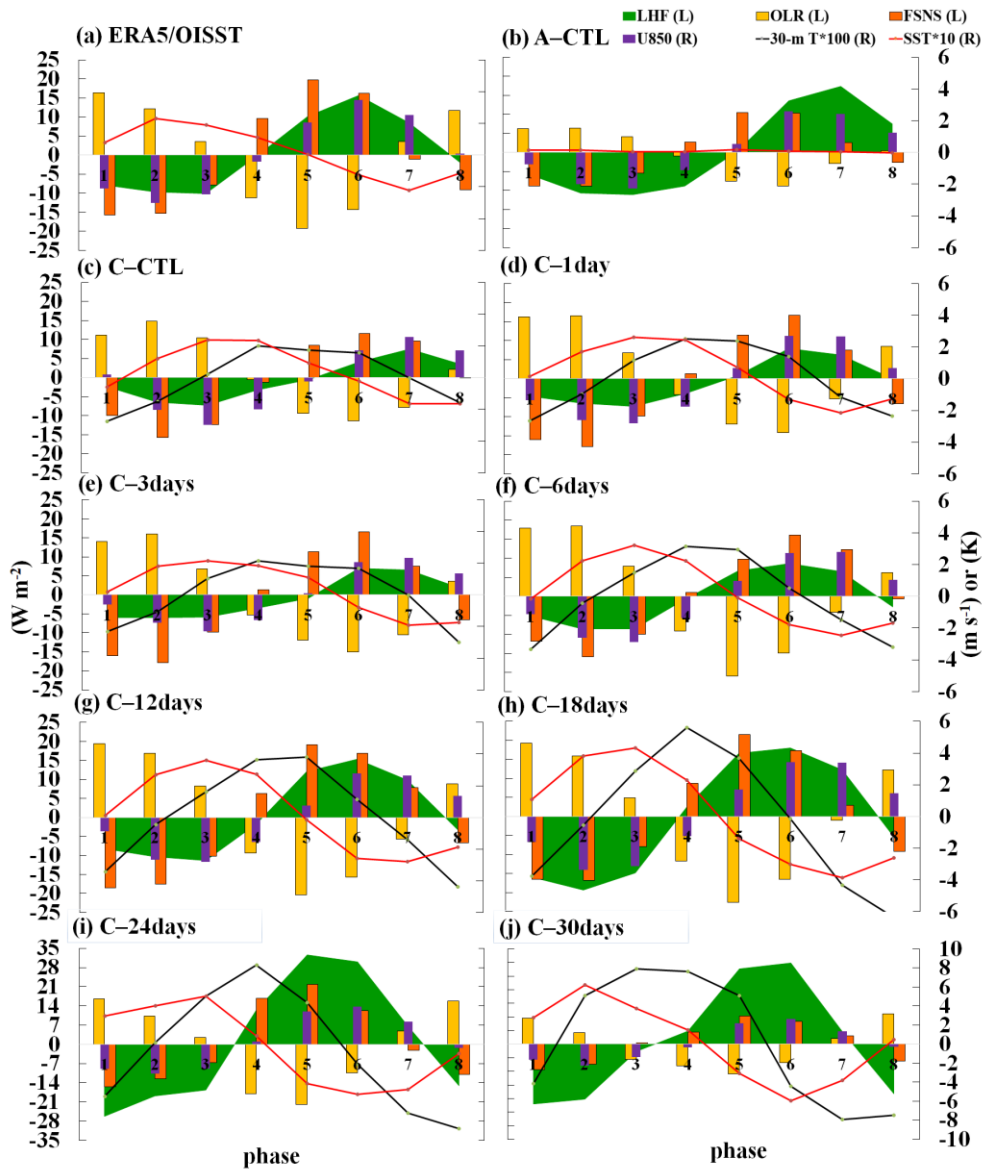
1085 **Figure 5.** Phase-vertical Hovmöller diagrams of 20–100-day specific humidity
 1086 (shading, g kg^{-1}) and air temperature (contoured, K) averaged over $5\text{--}20^\circ \text{S}$, $120\text{--}150^\circ$
 1087 E; solid, dashed, and thick-black curves are positive, negative, and zero values,
 1088 respectively. (a)–(j) are arranged in the same order as in Fig. 1 for NOAA/ERA5 and
 1089 all experiments.

1090



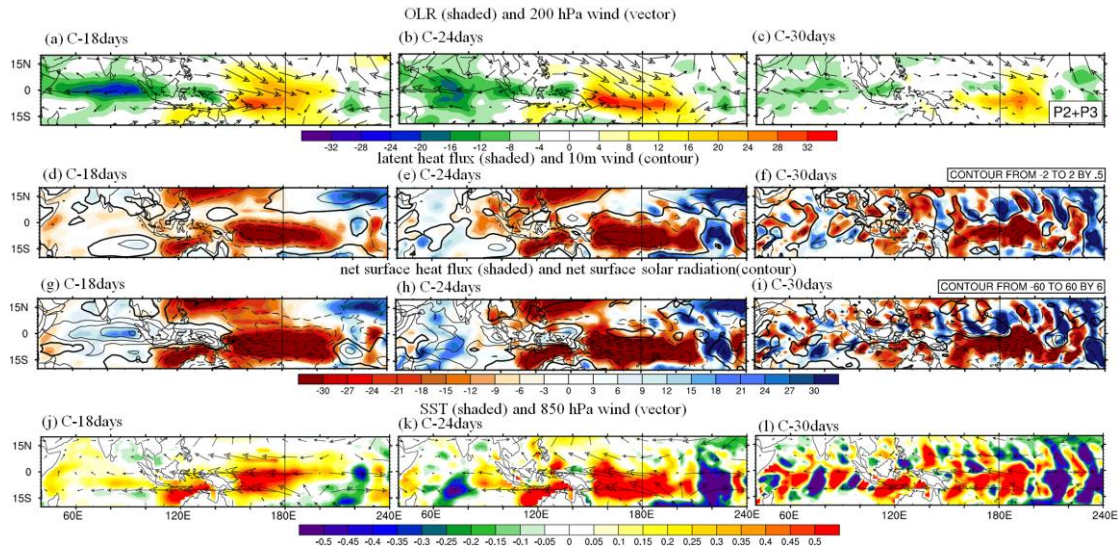
1092

1093 **Figure 6.** The 20–100-day filtered oceanic temperature (K, shaded and contour, interval
 1094 0.03) at phase 2–3 (Left column) and phase 4–5 (Right column) averaged over 0–15°
 1095 S between 0 and 60 m depth. (a)–(b) are from C–CTL, (c)–(d) are from C–1day, (e)–(f)
 1096 are from C–3days, (g)–(h) are from C–6days, (i)–(j) are from C–12days, (k)–(l) are
 1097 from C–18days, (m)–(n) are from C–24days, and (o)–(p) are from C–30days.



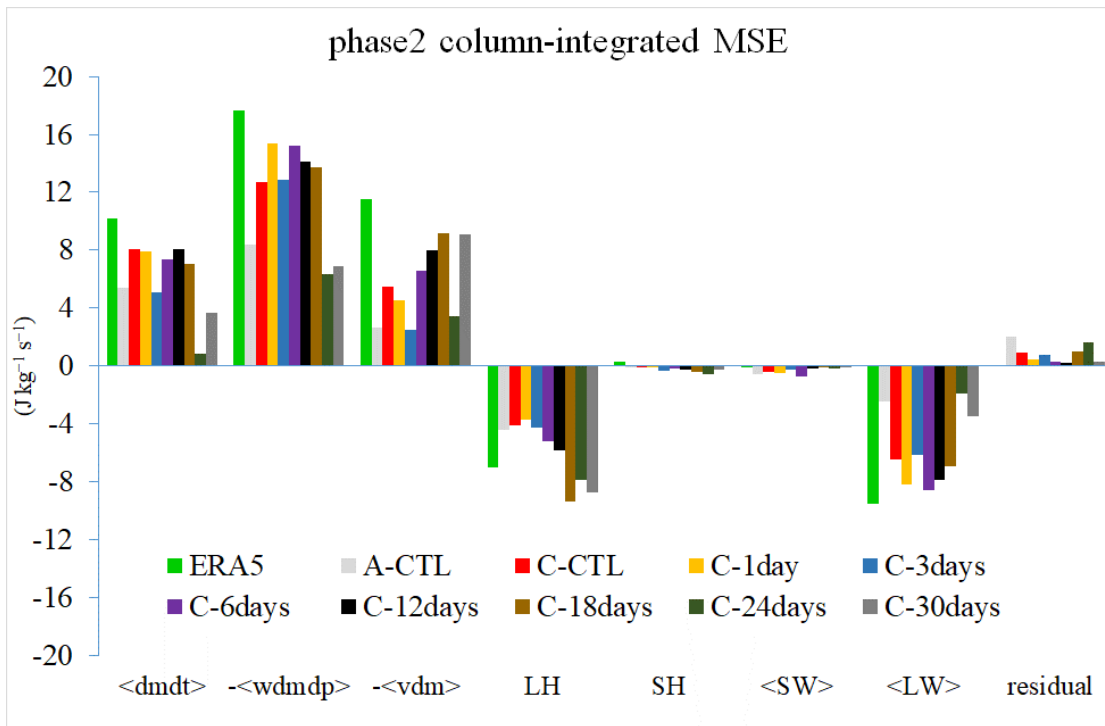
1098

1099 **Figure 7.** The lead-lag relationship between MJO-related atmosphere and SST
 1100 variation from phase 1 to 8 averaged within 110–130° E and 5–15° S. The variables
 1101 analyzed include 20-100-day filtered LHF, green shading), OLR (yellow bar chart),
 1102 FSNS, (orange bar chart), U850 (purple bar chart), 30-m T (multiplied by 100, black
 1103 line), and SST (multiplied by 10, orange line). Variables denoted with L (R)
 1104 by the left (right) y-axis. (a)–(j) are from ERA5/OISST reanalysis, A-CTL, C-CTL, C-
 1105 1day, C-3days, C-6days, C-12days, C-18days, C-24days, and C-30days, respectively.



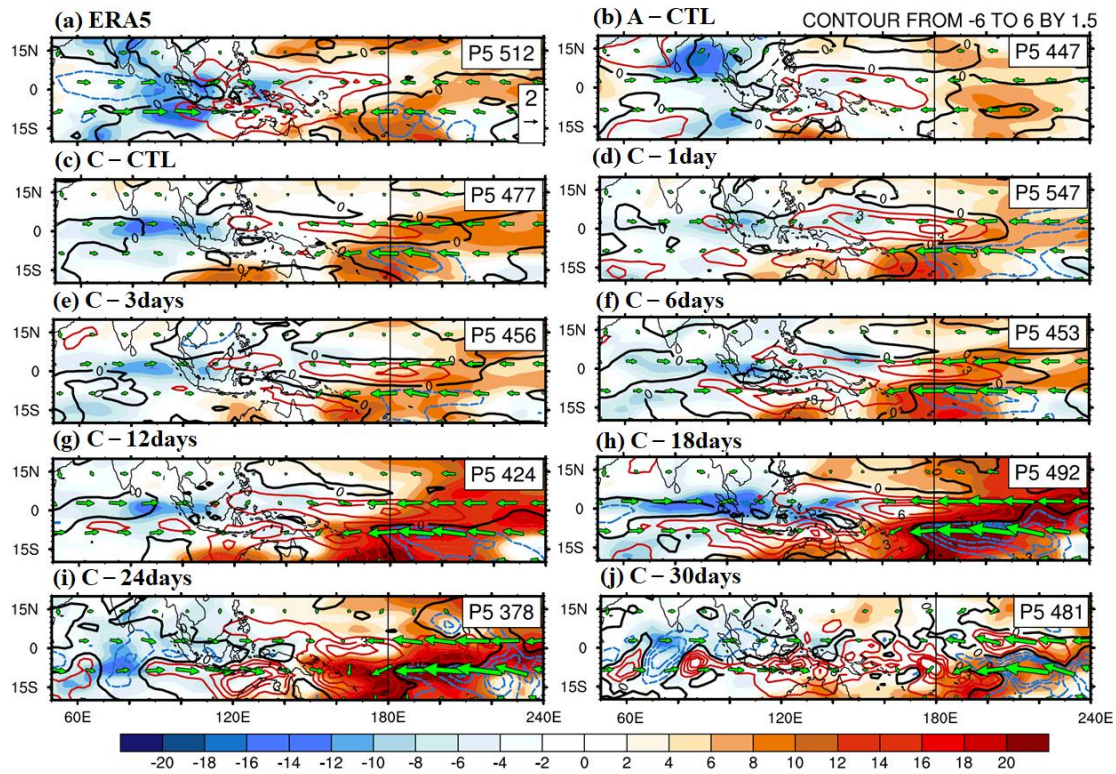
1106

1107 **Figure 8.** Averaged 20–100-day filtered fields at phase 2–3. (Upper row) OLR (W m^{-2} ,
 1108 shaded) and 200 hPa zonal and meridional wind anomaly (m s^{-1} , vector with reference
 1109 vector shown at the top right corner, latent heat flux (W m^{-2} , shaded, positive
 1110 representing upward), and 10-m wind anomaly (m s^{-1} , contour interval 0.5). (Second
 1111 row) net surface heat flux (W m^{-2} , shaded) and net solar radiation (W m^{-2} , contour
 1112 interval 6). (Third row) SST (K, shaded) and 850 hPa zonal and meridional wind
 1113 anomaly (m s^{-1} , vector with reference vector shown at the top right corner. The number
 1114 of days used to generate the composite is shown at the bottom right corner. (a), (d), (g)
 1115 and (j) are from C–18days; (b), (e), (h) and (k) are from C–24days, and (c), (f), (i) and
 1116 (l) are from C–30days, respectively. Solid, dashed, and thick-black lines represent
 1117 positive, negative, and zero values, respectively.



1119

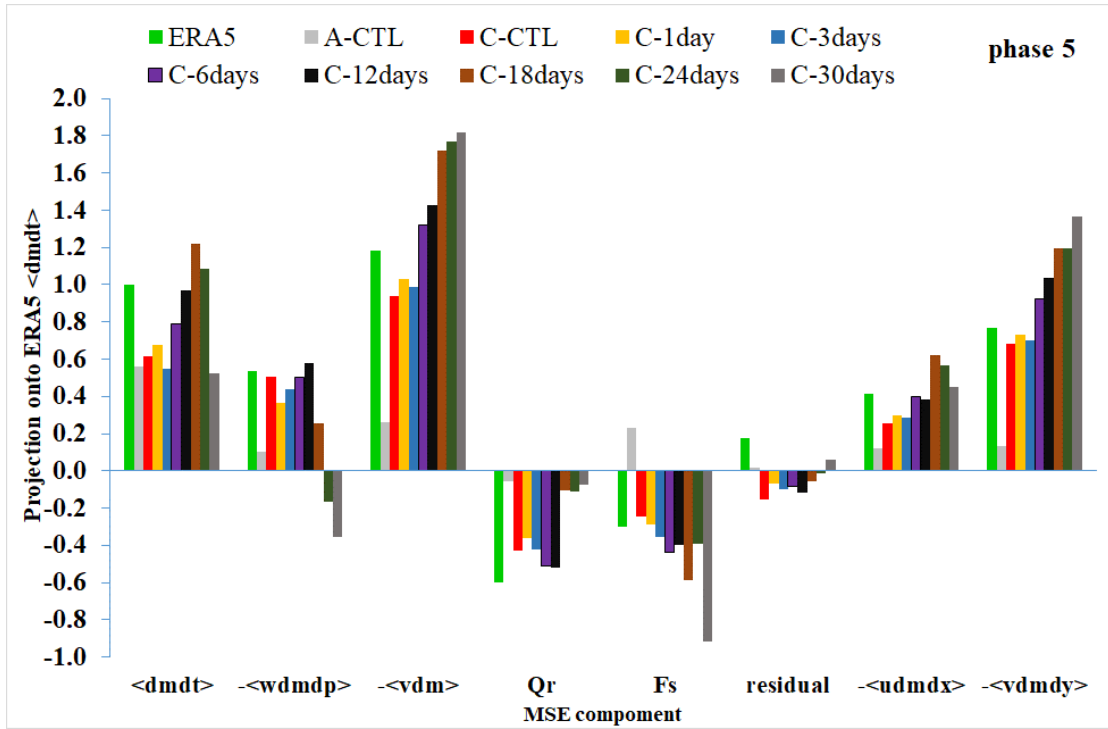
1120 **Figure 9.** Averaged 20–100-day filtered column-integrated MSE budget terms
 1121 (J kg⁻¹ s⁻¹) in 10° S–0° N/S, 120–150° E for ERA5 and all model simulations.
 1122 Colors represent different datasets: green for REA5, light gray for A–CTL, red, orange
 1123 and wathet blue for high-frequency experiments (C–CTL, C–1day, and C–3days,
 1124 respectively), purple, black, dark brown, dark green, and dark gray for low-frequency
 1125 experiments (C–6days, C–12days, C–18days, C–24days, and C–30days, respectively).
 1126 The bars from left to right represent MSE tendency ($\langle \text{dmdt} \rangle$), vertical MSE advection
 1127 ($-\langle \text{wdmdp} \rangle$), horizontal MSE advection ($-\langle \text{vdm} \rangle$), surface latent heat flux (LH),
 1128 surface sensible heat flux (SH), shortwave radiation flux ($\langle \text{SW} \rangle$), longwave radiation
 1129 flux ($\langle \text{LW} \rangle$), and residual terms.



1131

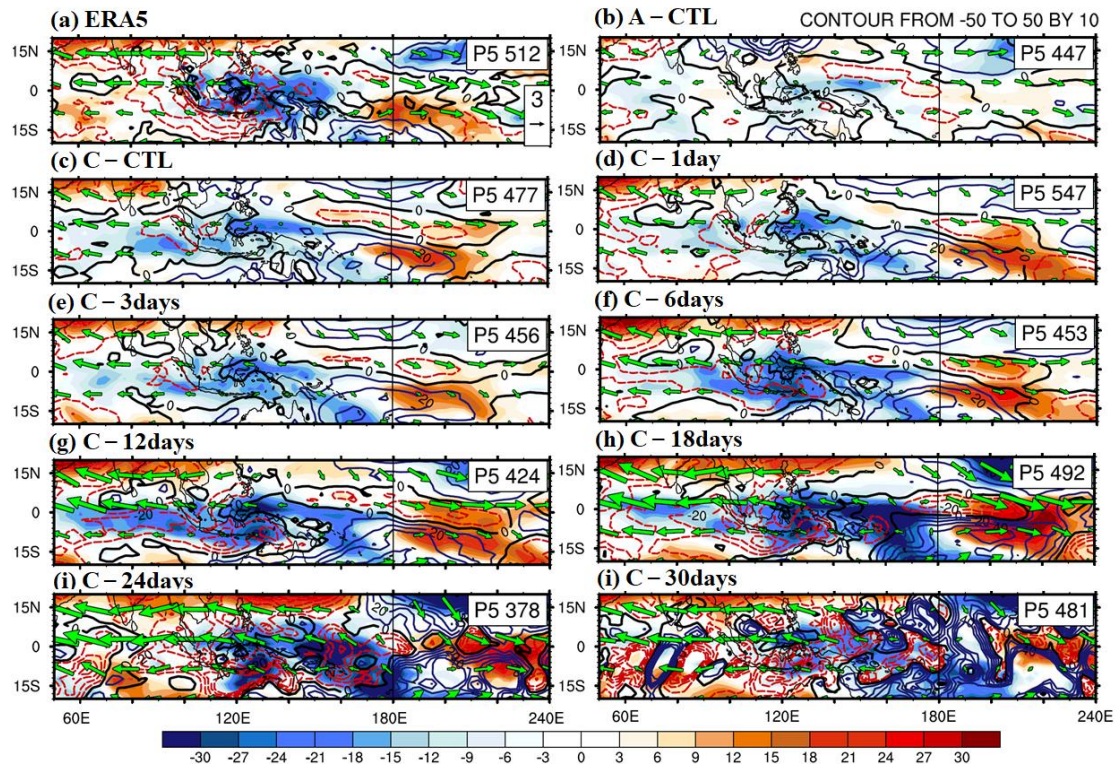
1132 **Figure 10.** Filtered the column-integrated MSE tendency ($\text{J kg}^{-1} \text{s}^{-1}$, shading),
 1133 precipitation (mm d^{-1} , contours interval 1.5) and 850-hPa wind (green vector,
 1134 reference vector 2 m s^{-1}) in phase 5: (a) ERA5, (b) A-CTL, (c) C-CTL, (d) C-1day,
 1135 (e) C-3days, (f) C-6days, (g) C-12days, (h) C-18days, (i) C-24days, and (i)
 1136 C-30days. Solid-red, dashed-blue, and thick-black curves represent positive, negative,
 1137 and zero values, respectively.

1138



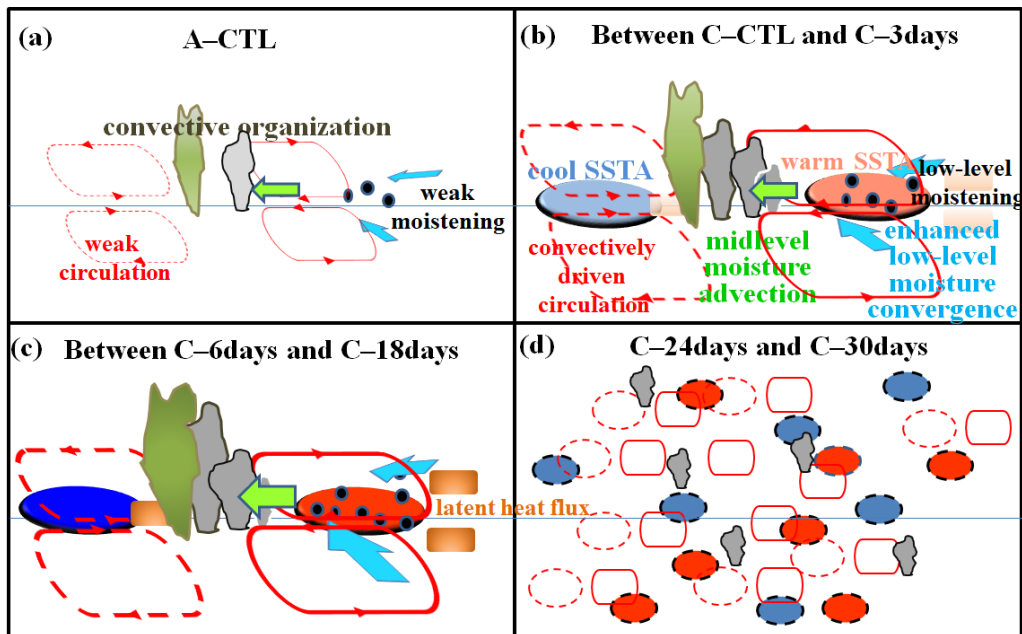
1139

1140 **Figure 11.** The projection of each MSE component onto the ERA5 column-integrated
 1141 MSE tendency at phase 5 over the MC (20° S– 20° N, 90 – 210° E): <dmdt>, -
 1142 <wdmdp>, -<vdm>, Qr, Fs, and residual; decomposition of horizontal MSE advection
 1143 to zonal and meridional advection (-<udmdt> and -<vmdy>).



1144

1145 **Figure 12.** Filtered column-integrated vertical ($\text{J kg}^{-1} \text{s}^{-1}$, shading) and horizontal
 1146 MSE advection ($\text{J kg}^{-1} \text{s}^{-1}$, contours interval 6.0), and 200-hPa wind (green vector
 1147 with reference vector 3 m s^{-1}): (a) ERA5, (b) A-CTL, (c) C-CTL, (d) C-1day, (e)
 1148 C-3days, (f) C-6days, (g) C-12days, (h) C-18days, (i) C-24days, and (j) C-30days.
 1149 Solid-blue, dashed-red, and thick-black curves represent positive, negative, and zero
 1150 values, respectively.



1152

1153 **Figure 13.** Schematic diagrams illustrate the anomalous circulation and moistening
 1154 processes during the eastward propagation of the MJO in experiments: (a) A-CTL, (b)
 1155 high-frequency SST feedback experiments (C-CTL, C-1day, and C-3days), (c) low-
 1156 frequency SST feedback experiments (C-6days, C-12days, and C-18days), and (d)
 1157 C-24days and C-30days experiment. In each panel, the horizontal line represents the
 1158 equator. The size of clustering gray clouds indicates the strength of convective
 1159 organization. A red ellipse indicates convection-driven circulation. In the coupled
 1160 simulations, light red (blue) filled ovals represent warm (cold) SST anomalies,
 1161 respectively, and grass green filled rectangle represent latent heat flux. Unresolved
 1162 convective processes are indicated by black dots representing low-level moisture
 1163 convergence. Low-level moisture convergence into the equatorial trough is shown by
 1164 light blue arrows, while midlevel moisture advection is represented by left-pointing
 1165 green arrows. The deeper colors or thicker lines on the map indicate stronger anomalies
 1166 of the MJO perturbations. Note: The concept of the figure is based on DeMott et al.
 1167 (2014).